Steel and Composite Structures, *Vol. 35, No. 3 (2020) 305-325*
DOI: https://doi.org/10.12989/scs.2020.35.3.305

Numerical study of the seismic behavior of steel frame-tube structures with bolted web-connected replaceable shear links

Ming Lian*[1,2], Qianqian Cheng[1a], Hao Zhang[1b] and Mingzhou Su[1,2c]

[1]*School of Civil Engineering, Xi'an University of Architecture & Technology, Xian 710055, China*
[2]*Key Lab of Structural Engineering and Earthquake Resistance, Ministry of Education (XAUAT), Xi'an 710055, China*

(*Received November 12, 2019, Revised March 12, 2020, Accepted April 3, 2020*)

Abstract. Beams of steel frame-tube structures (SFTSs) typically have span-to-depth ratios of less than five. This makes a flexural beam unsuitable for such an application because the plastic hinges at the beam-ends cannot be adequately developed. This leads to lower ductility and energy dissipation capacities of SFTSs. To address this, SFTSs with bolted web-connected replaceable shear links (SFTS-BWSLs) are proposed. In this structural system, a web-connected replaceable shear link with a back-to-back double channel section is placed at the mid-length of the deep beam to act as a ductile fuse. This allows energy from earthquakes to be dissipated through link shear deformation. SFTS and SFTS-BWSL buildings were examined in this study. Several sub-structures were selected from each designed building and finite element models were established to study their respective hysteretic performance. The seismic behavior of each designed building was observed through static and dynamic analyses. The results indicate that the SFTS-BWSL and SFTS have similar initial lateral stiffness and shear leg properties. The SFTS-BWSL had lower strength, but higher ductility and energy dissipation capacities. Compared to the SFTS, the SFTS-BWSL had lower interstory drift, base shear force, and story shear force during earthquakes. This design approach could concentrate plasticity on the shear link while maintaining the residual interstory drift at less than 0.5%. The SFTS-BWSL is a reliable resistant system that can be repaired by replacing shear links damaged due to earthquakes.

Keywords: steel frame-tube structure; web-connected replaceable shear link; hysteretic behaviors; dynamic behaviors; finite element analyses

1. Introduction

Traditional lateral seismic resistant systems dissipate the input seismic energy largely through the deformation of plastic hinges such as the flexural hinges at the beam-ends in moment-resisting frames (MRFs). Steel MRFs are reliable load-resisting systems with high ductility and significant energy dissipation capacity. After the Northridge and Kobe earthquakes, many investigations were conducted of the seismic behaviors and details of beam-to-column connections to improve the hysteretic performance of flexural hinges at the beam-ends in steel MRFs. Research results indicated that various approaches could improve the seismic performance of steel MRFs (Hu *et al*. 2014, Oh *et al.* 2015, Erfani *et al*. 2016, El-Khoriby *et al*. 2017, Sophianopoulos and Deri 2017, Fanaie and Moghadam 2019, Jiang *et al.* 2019; Zhang *et al.* 2019). The current design codes for steel MRFs consider plastic hinge deformation as an essential parameter in controlling performance level. In AISC 358-10 and FEMA-335D, it is stipulated that these beam-to-column connections be used in beams with clear span-to-depth ratios greater than 7 in special MRFs and 5 in intermediate MRFs such that the flexural plastic hinges at the beam-ends are of sufficient length.

In various high-rise structural systems, steel frame-tube structures (SFTSs) are effective structural systems because bending and transverse shear force are three-dimensionally resisted by the flange and web surfaces in the structure.

SFTSs can work as a huge vertical cantilever to resist overturning moments because the tube employs closely spaced perimeter columns interconnected by deep spandrel beams. This characteristic leads to the great lateral stiffness of SFTSs. The columns in the web and flange surfaces of SFTSs are typically spaced 3.0 to 4.0 m apart and the spandrel beam depths range from 0.6 to 1.5 m (Taranath 2011). This leads to beam span-to-depth ratios between 2.0 and 4.4. However, the application of a flexural beam makes SFTSs unsuitable because their beam span-to-depth ratios are typically less than 5. Under these conditions, the deformation of plastic hinges at the beam-ends cannot be fully determined. This leads to the limited energy dissipation capacity and poor seismic behavior of SFTSs. In SFTSs, the plastic deformation may first occur at the column-ends because of the great stiffness of the deep spandrel beams and the composite action of the floor slabs. This will increase the possibility of collapse under severe seismic loads. When the SFTSs are damaged during seismic events, and considering the means of dissipating energy through plastic hinge deformation, the reduced occupancy

*Corresponding author, Associate Professor
E-mail: lianming@xauat.edu.cn
[a] Ph.D. Student
[b] Ph.D. Student
[c] Professor

http://www.techno-press.org/?journal=scs&subpage=8
ISSN: 1229-9367 (Print), 1598-6233 (Online)

performance level and post-earthquake losses, repair difficulties, and costs hamper the application of this design technique. Accordingly, few researchers have focused on the seismic behavior of SFTSs; most studies seem interested only in elastic simplified analysis methods (Lee *et al*. 2001, Charney and Pathak 2008a, Charney and Pathak 2008b, Moon 2010, Kamgar and Rahgozar 2013, Malekinejad *et al*. 2016, Alavi *et al.* 2018). Moreover, the effect of blast phenomenon on structures and robust method have been proposed to determine the best location of belt truss system in tube structures (Kamga *et al*. 2018, Kamgar and Rahgozar 2019).

Shear links are the dissipative component in eccentrically braced frames (EBFs). The current studies on the performance of shear links indicate that they have reliable hysteretic behaviors and energy dissipation capacities via shear deformation (Dusicka *et al.* 2010, Shayanfar *et al.* 2012, Okazaki and Engelhardt 2015, Lian *et al.* 2017, Mohammadrezapour and Danesh 2018, Silvia 2018). Moreover, Mansour et al. proposed bolted web-connected replaceable shear links in EBFs to improve the repairability of the structures. Cyclic loading test results for full specimens indicated that the bolted web-connected replaceable shear links showed good ductile and inelastic behaviors. Considering the characteristics of bolted web-connected replaceable shear links, they can be proposed as ductile fuses where damage concentrates on these links while other components remain elastic during seismic loads. In steel frame-tube structures with replaceable shear links (SFTS-SLs), the replaceable shear links can be placed at the mid-length of the deep beams with low span-to-depth ratios as the ductile fuse. The replaceable shear link has lower shear capacity than that of the beam, such that the seismic energy is dissipated through the link shear deformation, which is similar to that of the EBFs. In SFTS-SLs, the section of the replaceable shear link is independent from the spandrel beam, leading to the decoupled design of strength and stiffness for this structure. Concentrating seismic force on replaceable shear links in SFTS-SLs while other components remain in an elastic state reduces the requirement for the development of flexural hinges at the beam-ends in deep spandrel beams. In addition, there is low residual drift for SFTS-SLs following the seismic loads because of their great lateral stiffness. Replacing damaged shear links after earthquakes can achieve the goal of seismic rehabilitation for SFTS-SLs and reduce the cost of post-earthquake retrofitting.

Dolatshahi *et al.* proposed new hybrid energy dissipated steel MRF systems that combine shear fuses with reduced beam sections (RBS) in the MRFs. Different shapes of shear links were considered and experimental tests were conducted to investigate the cyclic behaviors of the single span-single story specimens of this system (Mahmoudi *et al.* 2016, Dolatshahi *et al.* 2018). However, these investigations focused on the hysteretic behaviors of single-span and single-story frames; the hysteretic behaviors of steel MRFs with beam span-to-depth ratios of less than 4 and the seismic performance of buildings during dynamic loads were not considered. Moreover, the seismic behaviors of steel MRFs with shear fuses were not compared to those of the conventional steel MRFs without a reduced beam section (RBS). In this study, replaceable bolted web-connected links with back-to-back double channel sections were considered as the shear fuses in SFTS-SLs (SFTS-BWSLs). Thirty-story conventional SFTS and SFTS-BWSL buildings were designed and several sub-structures were selected from the two designs to study and compare the seismic behaviors of the SFTS and SFTS-BWSL structures. ABAQUS finite element models (FEMs) of these sub-structures were established to study their hysteretic performance under horizontal cyclic loads. The FEMs of the SFTS and SFTS-BWSL buildings were established using SAP2000. Static pushover and dynamic analyses were used for seismic behavior comparisons of the two buildings.

2. Design concepts and details

In steel MRFs, the flexural plastic hinges at the beam-ends are the main energy dissipative mechanism. As shown in Fig. 1, the nominal plastic shear strength of beam section V_{pb} is calculated by Eq. (1), corresponding to the nominal plastic flexural strength of beam section M_{pb}, as follows

$$V_{pb} \le \frac{2M_{pb}}{L_n} \tag{1}$$

where L_n is the clear span of the beam.

According to Fig. 1 and Eq. (1), the shear force for a beam increases by decreasing the beam length. In SFTSs, the close spacing of external columns results in much greater shear force demands on the beams relative to those used in conventional steel MRFs. This leads to the greater section depths of the spandrel beams in SFTSs. Increasing the web thickness or depth of a beam section can provide the required shear capacity for beams; this leads to increased M_{pb}. These also increase the required capacity demands for other structural components leading to the overdesign for SFTSs. In SFTS-SLs, placing a replaceable shear link at the mid-span of a beam can provide sufficient shear and energy dissipation capacity while greatly reducing the beam shear capacity requirements. Fig. 2 shows the details of a bolted web-connected replaceable shear link with back-to-back double channel sections in a SFTS-BWSL. As shown in Fig. 1, because the theoretical bending moment caused by the lateral loads is zero at the mid-span of the beam, using this approach of a replaceable shear link at this location will not decrease the structure lateral stiffness.

3. Designs of the SFTSs and SFTS-BWSLs

In this section, 30-story SFTS and SFTS-BWSL buildings were designed based on the design codes of GB50010-2010, JGJ99-2015 and AISC 358-10. The site for these two buildings was characterized by peak ground acceleration (PGA) of 0.2 g with a 10% exceedance probability during a 50-year period and moderately firm ground conditions. The story height of the two buildings

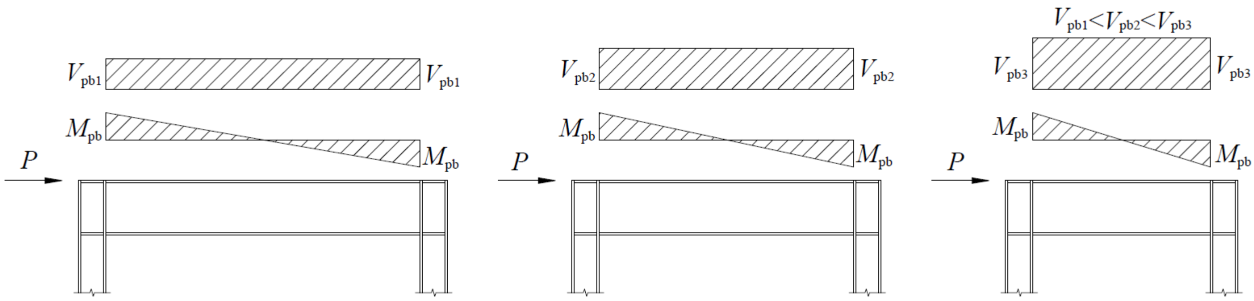

Fig. 1 Shear and moment demands for beams in SFTSs

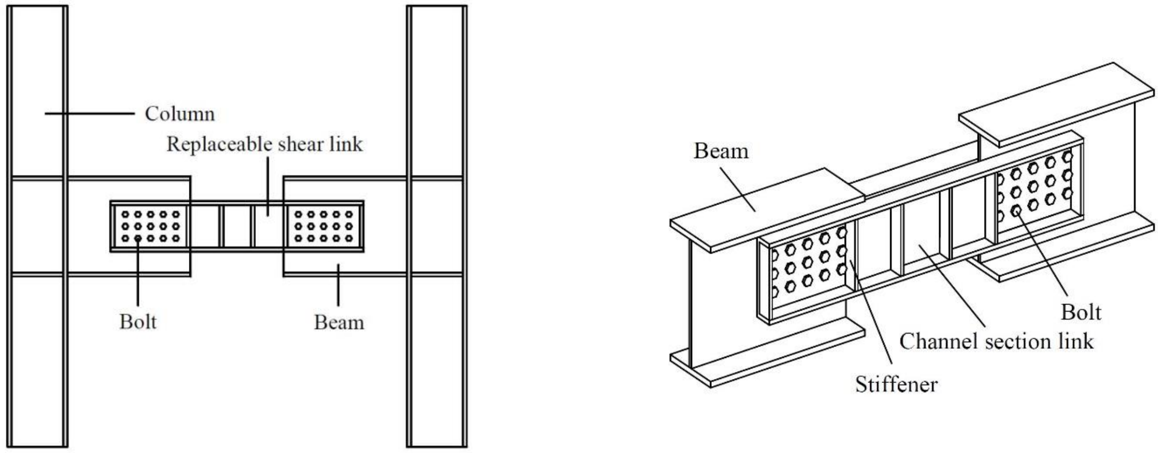

Fig. 2 Concept of the SFTS-BWSLs

Table 1 Structural component sections in the 30-story SFTS building

Story	Beams	External columns	Corner columns	Inner Beams	Inner columns
1-5	H850×350×20×30	H500×400×20×25	Box900×900×40	H700×300×25×30	Box800×800×40
6-10	H820×300×20×30	H480×380×20×25	Box850×850×40	H700×300×25×30	Box750×750×35
11-15	H800×300×20×30	H470×360×20×25	Box800×800×40	H700×300×25×30	Box700×700×35
16-20	H750×300×20×25	H450×350×20×25	Box750×750×35	H700×300×25×30	Box650×650×30
21-25	H720×300×20×25	H420×320×20×25	Box700×700×35	H700×300×25×30	Box600×600×30
26-30	H650×300×20×25	H400×300×20×25	Box650×650×30	H700×300×25×30	Box550×550×30

“H” refers to the welded H-shaped section, the following numbers are the section depth (h), flange width (b_f), web thickness (t_w) and flange thickness (t_f), with unit of mm.

was 3.3 m. There were nine bays in both the x-direction and y-direction and the spans were 3.0 m. The shear capacities of the bolted web-connected shear links were lower than those of the beams. Considering that the significant shear lag effects in the SFTSs result in the high shear strength for beams in the beam-to-corner and the adjoining bays, the shear links were employed in the third and seventh bays in the SFTS-BWSL building such that it could not increase the shear lag effects of the structure. Fig. 3 shows the details of the two buildings with the plan and elevation data. A value of 4.8 kN/m^2 was considered for the dead load of the floors and roofs. The floor live load, roof live load, and snow load were 2, 0.5, and 0.25 kN/m^{2,} respectively. The shear link lengths were 700 mm in the SFTS-BWSL building and the two buildings had the same cross sections of beams, columns, and reinforced concrete (RC) slabs. All structural components used Q345 steel with nominal yield strength of 345 MPa. The cross sections of the structural components in the SFTS and SFTS-BWSL buildings are summarized in Table 1 and Table 2, respectively. In the SFTS-BWSL building, the $e/(M_p/V_p)$ ratios of the shear links ranged from 1.02 to 1.12, where M_p and V_p are the nominal plastic flexural strength and nominal plastic shear strength of the link, respectively.

Table 2 Structural component sections in the 30-story SFTS-BWSL building

Story	Shear links	Beams	External columns	Corner columns	Inner Beams	Inner columns
1	C450×125×8×20					
2	C440×125×8×20					
3	C430×125×8×20	H850×350×20×30 (Story 1-5)	H500×400×20×25 (Story 1-5)	Box900×900×40 (Story 1-5)	H700×300×25×30 (Story 1-5)	Box800×800×40 (Story 1-5)
4	C420×125×8×20					
5	C410×125×8×20					
6	C430×125×8×20					
7	C420×125×8×20					
8	C420×110×8×22	H820×300×20×30 (Story 6-10)	H480×380×20×25 (Story 6-10)	Box850×850×40 (Story 6-10)	H700×300×25×30 (Story 6-10)	Box750×750×35 (Story 6-10)
9	C410×110×8×22					
10	C400×110×8×22					
11	C390×110×8×22					
12	C380×110×8×22					
13	C410×100×7×22	H800×300×20×30 (Story 11-15)	H470×360×20×25 (Story 11-15)	Box800×800×40 (Story 11-15)	H700×300×25×30 (Story 11-15)	Box700×700×35 (Story 11-15)
14	C400×100×7×22					
15	C390×100×7×22					
16	C380×100×7×22					
17	C370×100×7×22					
18	C400×100×6×20	H750×300×20×25 (Story 16-20)	H450×350×20×25 (Story 16-20)	Box750×750×35 (Story 16-20)	H700×300×25×30 (Story 16-20)	Box650×650×30 (Story 16-20)
19	C390×100×6×20					
20	C380×100×6×20					
21	C370×100×6×20					
22	C360×100×6×20					
23	C350×100×6×20	H720×300×20×25 (Story 21-25)	H420×320×20×25 (Story 21-25)	Box700×700×35 (Story 21-25)	H700×300×25×30 (Story 21-25)	Box600×600×30 (Story 21-25)
24	C390×100×5×16					
25	C370×100×5×16					
26	C330×100×5×16					
27	C320×100×5×16					
28	C340×100×4×14	H650×300×20×25 (Story 26-30)	H400×300×20×25 (Story 26-30)	Box650×650×30 (Story 26-30)	H700×300×25×30 (Story 26-30)	Box550×550×30 (Story 26-30)
29	C330×100×4×14					
30	C320×100×4×14					

"C" refers to the welded channel-shaped section, the following numbers are the section depth (h), flange width (b_f), web thickness (t_w) and flange thickness (t_f), with unit of mm.

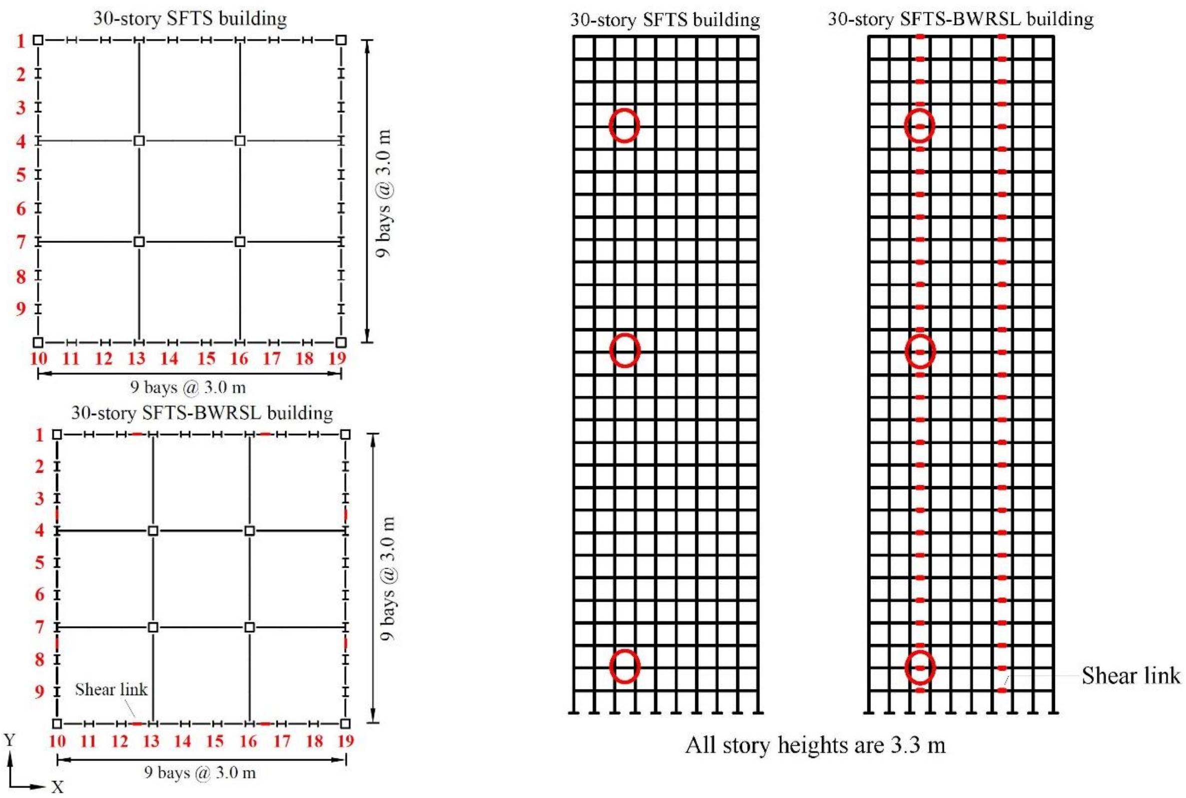

Fig. 3 Building plan and elevation views

Table 3 Designations of the FEMs

Sub-structures	Designation		
	2nd story	16th story	26th story
SFTS building	SFTS1	SFTS2	SFTS3
SFTS-BWSL building	SFTS-BWSL1	SFTS- BWSL2	SFTS- BWSL3

Table 4 Geometries of stiffeners in FEMs (unit: mm)

FEMs	Link web stiffeners			Column stiffeners		
	Height	Width	Thickness	Height	Width	Thickness
SFTS1	–	–	–	450	190	30
SFTS2	–	–	–	400	165	25
SFTS3	–	–	–	350	140	25
SFTS-BWSL1	400	117	20	450	190	30
SFTS-BWSL2	336	93	18	400	165	25
SFTS-BWSL3	298	95	16	350	140	25

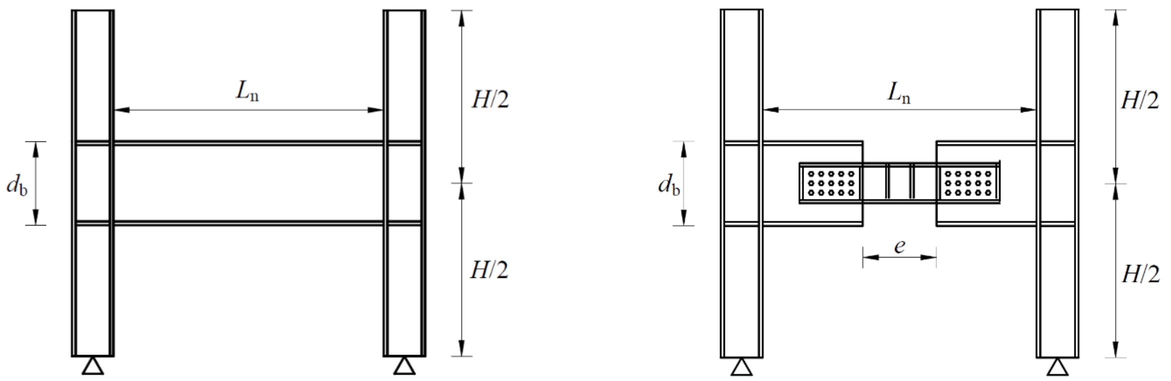

(a) SFTS (b) SFTS-BWSL

Fig. 4 Selected sub-structures

4. Hysteretic analyses

4.1 finite element models

To investigate the hysteretic performance of the SFTS and SFTS-BWSL buildings with beam span-to-depth ratios less than 5, three SFTS sub-structures and three SFTS-BWSL sub-structures were selected from the two 30-story buildings. Fig. 4 shows the SFTS and SFTS-BWSL sub-structures, in which L_n is the clear span, d_b is the beam depth, H is the story height, and e is the shear link length. Because the moment caused by the lateral force is theoretical zero at the moment inflection point placed on the mid-length of column, so half length of the column was selected in the sub-structures, and the position at the mid-length of column can be seen as a hinge point. For the sub-structures, considering the effects of different beam span-to-depth ratios (L_n/d_b) on the hysteretic performance, an L_n/d_b of 3.0, 3.5, and 4.0 was selected. Based on these, as shown in Fig. 3, the proposed sub-structures were chosen from the 2nd, 16th and 26th stories of each building.

The FEMs of the selected sub-structures were established using ABAQUS and the corresponding designations of these FEMs are summarized in Table 3. In the selected sub-structures, the full-depth web stiffeners were provided on link web in each channel section, and column stiffeners were also considered. Table 4 shows the geometries of these stiffeners in each FEM. To reduce the computational time and because of the fact that the shell elements are capable of properly capturing the effects of local buckling (Berman and Bruneau 2008, Prinz and Richards 2009, Ohsaki and Nakajima 2012, Chacón *et al.* 2019), the FEMs were developed using shell S4R elements for links, beams, columns, and stiffeners. Solid C3D8R elements were employed for the bolts. Moreover, the details of the stiffeners and welds were not explicitly modeled in the FEMs. The finite element sizes in the shear links and bolts were 20 and 5 mm, respectively. The finite element sizes in the columns, beams, and column-stiffeners were 40 mm. The FEMs and meshing details are shown in Fig. 5(a). In these FEMs, the contact relationship is established between the deep spandrel beam web, shear link web, and

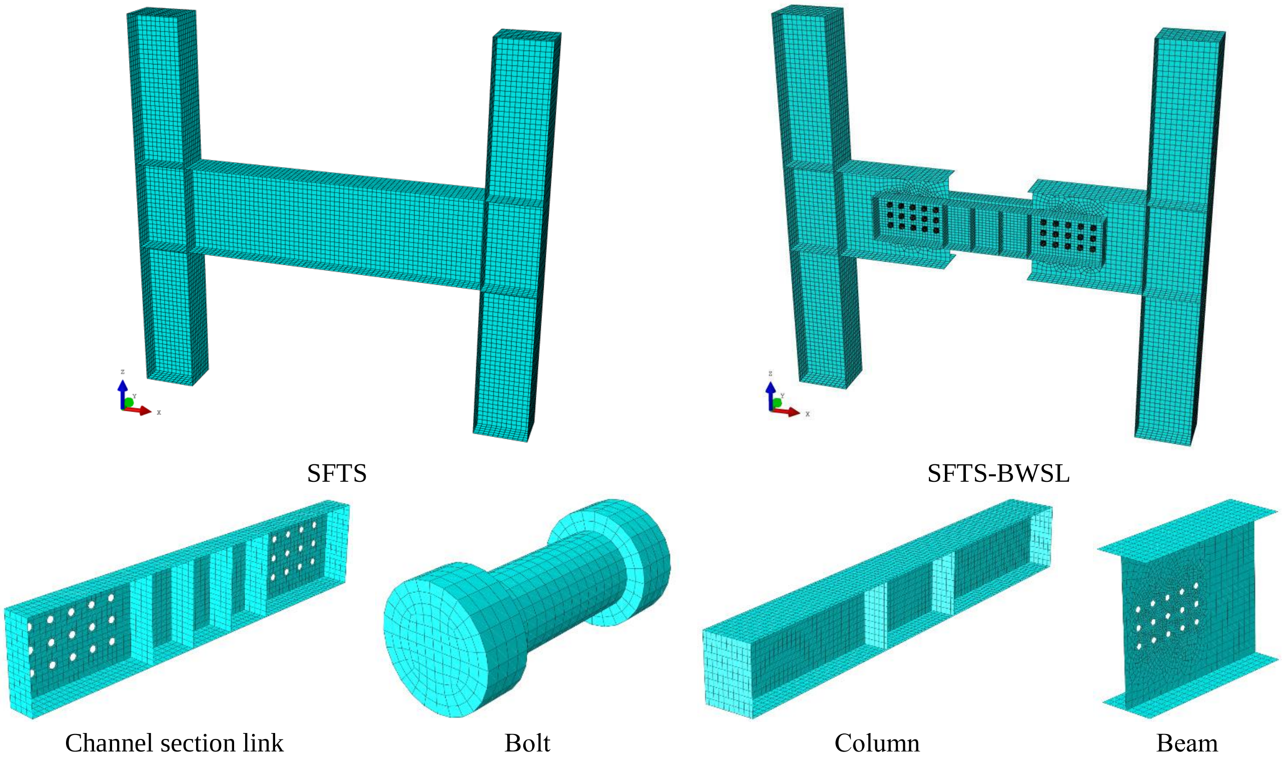

(a) FEMs and meshing densities

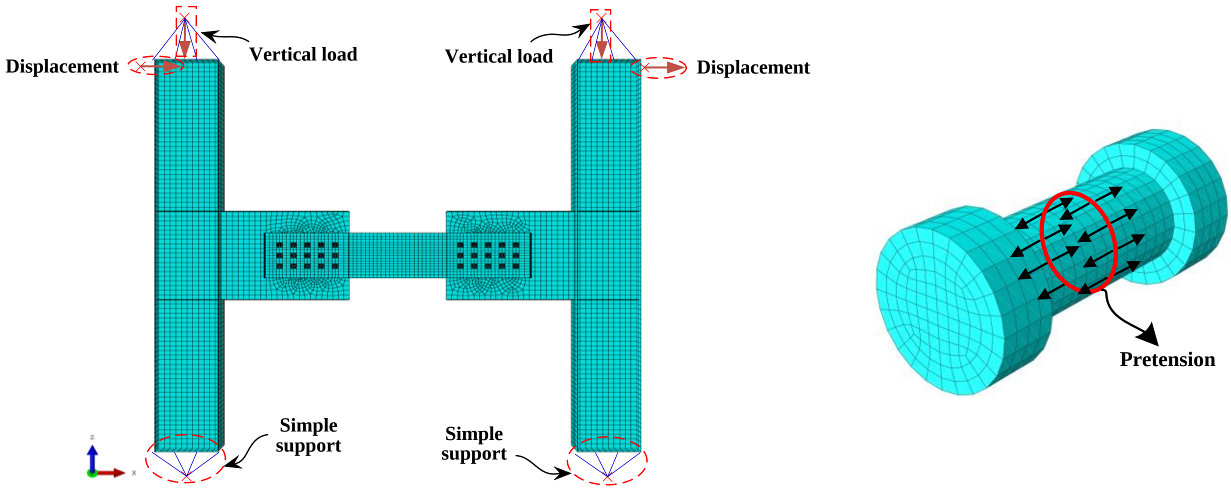

(b) Loading boundaries

Fig. 5 FEM details

bolts. The tangential behavior with a "Penalty" friction formulation and the normal behavior with a "Hard contact" were selected in the contact property; the tangential friction coefficient considered on the interfaces between the plates was taken as 0.45 and preload loads of 355 kN were applied to the bolts considering the requirements in GB50017-2017.

The hinged boundary constraint was applied to the bottom of the columns in the FEMs and the out-plane deformation of beams and columns was restrained, as shown in Fig. 5(b).

The von Mises yield surface and an associated flow rule were used to model the plasticity. The multi-linear kinematic hardening model has widely used in elastic-plastic analysis for steel structures. This model considers the Bauschinger effect and only few parameters should be defined. It makes the multi-linear kinematic hardening model has a significant calculation efficiency. Therefore, multi-linear kinematic hardening model was used in the analysis for the steel plates in the FEMs, which is shown in Fig. 6. In this stress–strain response for the steel, ε_y and ε_u are the yield and ultimate strains, respectively, and σ_y and σ_u are the yield and ultimate stresses, respectively. For the steel in the FEMs, nominal yield strength (f_y=345 MPa for Q345 steel) was adopted, including the steel in the shear links, columns, beams, link web stiffeners, and column stiffeners. The elastic modulus E and Poisson's ratio ν for the steel in the FEMs were assumed to be 206,000 MPa and 0.3, respectively. Considering the properties of Q345 steel, the tangent modulus E_t was equal to $0.01E$. Moreover, for the bolts, the nominal yield stress and ultimate stress of the steel were 900 MPa and 1000 MPa, respectively. The elastic modulus E and Poisson's ratio ν were 206,000 MPa and 0.3, respectively. The stress–strain relationship, which is shown in Fig. 6, was also considered as the hardening behavior for the bolt steel. In the hysteretic analyses, the influence of initial imperfections and residual stress were not considered and P-delta effects were included.

Firstly, a vertical axial load equal to the axial pressure ratio of 0.3 was conducted on the top of each column to consider the vertical loads transferred from the superstructure. Subsequently, displacement-controlled loadings were applied at the top of each column, as shown in Fig. 5(b). The FEMs were loaded under a horizontal displacement control for one cycle with a magnitude of $\pm0.25\Delta_y$, $\pm0.50\Delta_y$, and $\pm0.75\Delta_y$ before yielding and three cycles with a magnitude of $\pm\Delta_y$, $\pm2\Delta_y$, $\pm3\Delta_y$, $\pm4\Delta_y$,... $\pm\Delta_{target}$ after yielding, in which Δ_y and Δ_{target} are the horizontal yield displacement and target displacement, respectively.

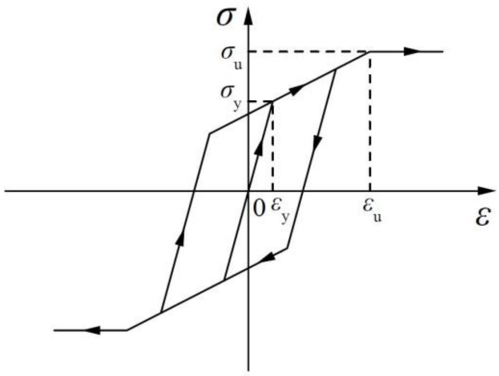

Fig. 6 Stress–strain relations

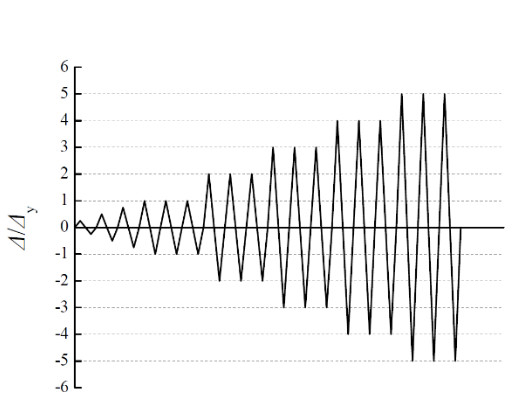

Fig. 7 Loading history for the FEM analyses

The Δ_{target} used a displacement corresponding to the 5% story drift for the FEMs in the analyses (Ellingwood 2001). Fig. 7 shows the loading history, where Δ is the horizontal displacement.

4.2 Model verification

Test results of two shear links available in the literature were compared to the finite element analytical results to verify the modeling approach discussed in this paper. Specimen UT-1B was a full-scale shear link with a pair of back-to-back double channel sections bolted on either side of the web of the connecting floor beam, which was tested by Mansour *et al*. (2011). Specimen CB3 was a large-scale back-to-back double channel section shear link tested by Ji *et al.* (2017). The FEMs of these two test specimens were established by the modeling assumptions discussed in this paper based on the details of the test specimens. Fig. 8 shows the FEMs of the two specimens using ABAQUS, in which the links, beams, and stiffeners used shell elements and the bolts used solid elements. In these FEMs, the contact relationship was established between the deep spandrel beam web, shear link web, and bolts. The tangential behavior with a "Penalty" friction formulation and the normal behavior with a "Hard contact" were selected in the contact property. The preload loads were applied to the bolts using the test values and the plate material, boundary conditions, and loading patrol were consistent with those of the tests. Figs. 9(a) and 9(b) compare the hysteretic curves and deformed geometry of the test specimens and their FEMs. In Fig. 9(a), the comparison of hysteretic curves shows that there are slight differences between the numerical analysis results and test results in both positive and negative zones. For the test specimen UT-1B, the strength decreased because of the severe link web fracture at the large displacement loading level. However, the FEM did not consider the effects of metal damage and fracture. Therefore, no fracture occurred within the link web in the FEM. Accordingly, this result in the higher strength of the FEM than that of the specimen UT-1B at last. For specimen UT-1B, the maximum base shear force was 1587.1 kN obtained from the numerical analysis results, which is 7.4% higher than the test result of 1478.0 kN. For specimen CB3, the numerical analysis result of maximum base shear force was 905.3 kN, which is 2.8% higher than the test result of 880.4 kN. Moreover, it is an iterative process with tension and pressure in diagonal direction for the link web under the cyclic shear strength. This leads to the link web buckling occurred in both test specimens and FEMs. Actually, on the whole, the comparison shows that the finite element analysis curves were fully spindle-shaped and in good agreement when compared to the test curves. Moreover, the comparison results indicated that the FEMs could properly simulate the link web yielding and local buckling described in the test specimens. Therefore, the simulation results are considered to be in good agreement with the test results.

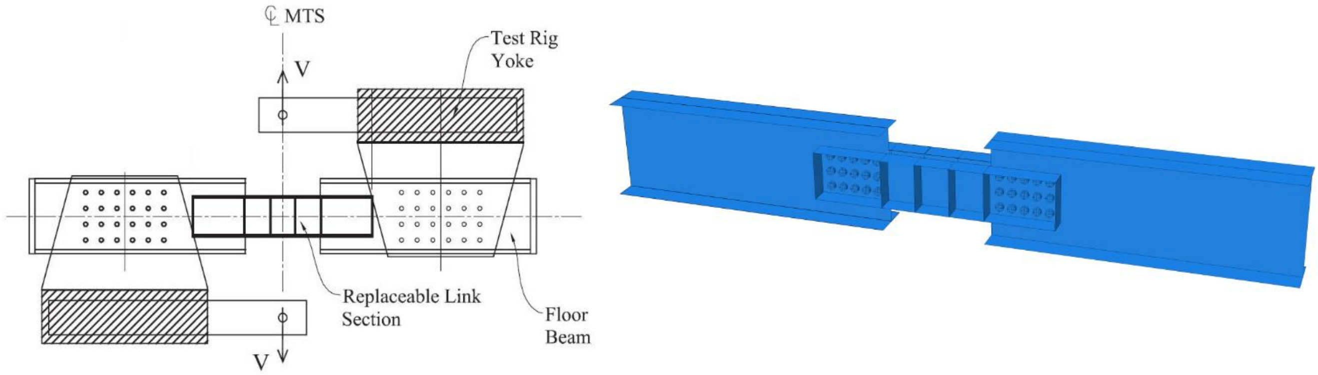

(a) Test specimen UT-1B and FEM

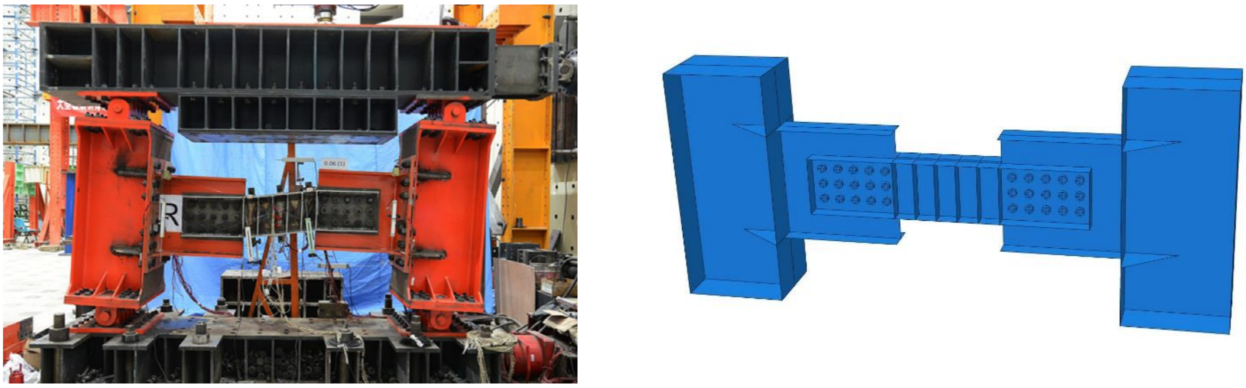

(b) Test specimen CB3 and FEM

Fig. 8 FEM of the test specimen

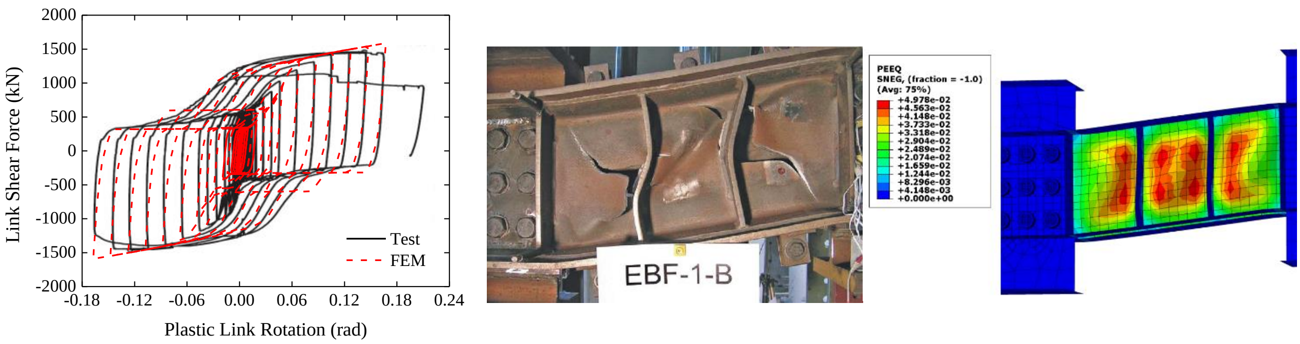

(a) Specimen UT-1B

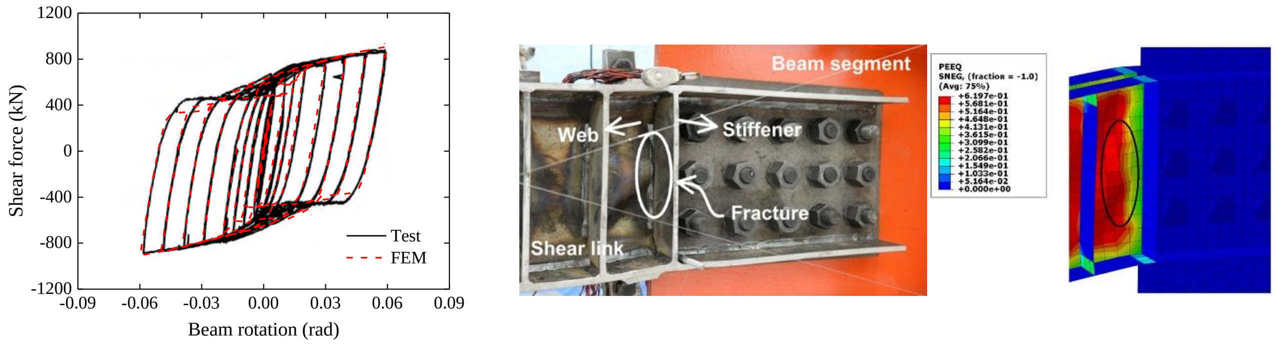

(b) Specimen CB3

Fig. 9 Hysteretic curves and deformed geometry comparison

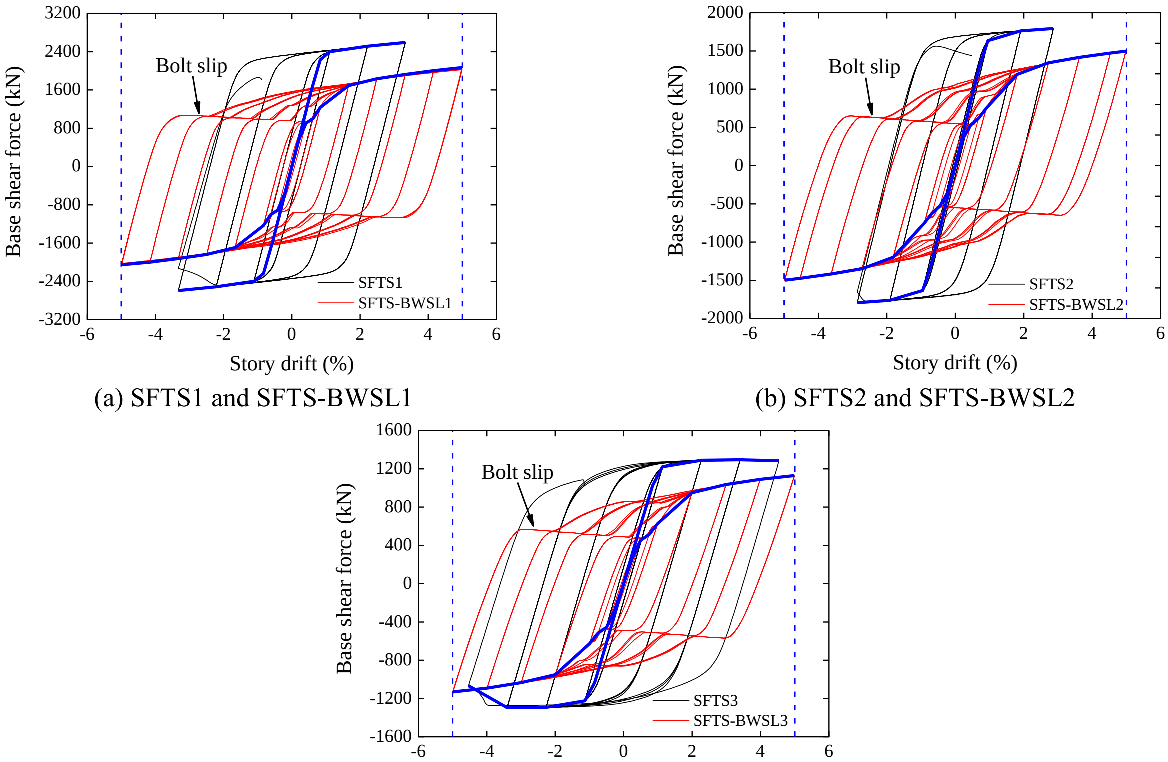

(a) SFTS1 and SFTS-BWSL1 (b) SFTS2 and SFTS-BWSL2

(c) SFTS3 and SFTS-BWSL3

Fig. 10 Hysteretic curves

4.3 Analytical results

4.3.1 Hysteretic curves

The hysteretic responses from the cyclic loading analyses for all FEMs are shown in Fig. 10. In all cases, the maximum story drifts of SFTS-BWSL FEMs could reach 5% story drift, showing plastic behaviors and did not result in any strength degradation. The hysteretic loops of SFTS-BWSL FEMs indicated that bolt slip occurred at the link-to-beam connections. However, these hysteretic loops were plump, which shows that they had significant energy dissipation capacities. However, for SFTS FEMs, their maximum story drifts were much less than 5% because local buckling occurred at the column flange next to the column-to-beam connections and the beam web and flange at the beam-ends. This resulted in obvious strength degradation for SFTS FEMs.

4.3.2 Load-carrying capacity

The yield strength P_y and maximum strength P_{max} of all FEMs are shown in Table 5. The P_y of the STFS-BWSL FEMs is obviously less than that of the corresponding SFTS FEMs. The P_y of SFTS-BWSL FEMs was at least 47.0% less than that of SFTS FEMs. This strength reduction in P_y is because the shear link had a lower shear capacity than that of the deep spandrel beam, leading to a lower P_y for the SFTS-BWSL. However, when these FEMs were damaged or reached the target story drift, the differences in P_{max} between the SFTS-RSL FEMs and SFTS FEMs were smaller. The P_{max} of SFTS-BWSL FEMs was at least 11.0% lower than that of SFTS FEMs. This shows that the SFTS-BWSL had a slightly lower P_{max} than that of the SFTS. Moreover, it is notable that the P_{max}/P_y ratios of the SFTS FEMs ranged from 1.06 to 1.10 but were 1.67 to 1.99 for the SFTS-BWSL FEMs. This indicated that the SFTS achieves a minor increase in seismic load resistance but the SFTS-BWSL had more stable hardening behaviors.

4.3.3 Stiffness

The initial elastic lateral stiffness K_e of the FEMs is shown in Table 6, including the K_e in the positive and negative loading directions. It shows that the K_e of each FEM was almost identical in the two loading directions. The K_e of SFTS-BWSL FEMs was slight lower than that of SFTS FEMs. This indicated that placing a shear link at the mid-span of the beam did not significantly reduce the initial elastic lateral stiffness of the frame. It had nearly no effect on the initial lateral stiffness of the frame using a shear link at the mid-span of beam where the flexural demand resulting from the lateral load is zero in theory.

4.3.4 Ductility capacity

The ductility of each FEM can be determined by the ductility coefficientμ, which can be calculated as $\mu=\theta_{max}/\theta_y$, where θ_y and θ_{max} are the yield and maximum story drift, respectively. Table 7 presents the ductility coefficient μ of all FEMs. It shows that the μ values were the same in the positive and negative loading directions for each FEM.

Table 5 Load-carrying capacities of the FEMs

Load directions	Base shear force (kN)	SFTS FEMs			SFTS-BWSL FEMs		
		SFTS1	SFTS2	SFTS3	SFTS-BWSL1	SFTS-BWSL2	SFTS-BWSL3
Positive	P_y	2387.32	1622.61	1212.21	1230.88	752.71	642.55
	P_{max}	2529.77	1792.94	1293.65	2067.87	1496.44	1129.5
	P_{max}/P_y	1.06	1.10	1.07	1.68	1.99	1.79
Negative	P_y	2399.26	1633.69	1224.43	1232.67	752.71	626.05
	P_{max}	2539.39	1793.19	1295.70	2054.04	1498.49	1130.04
	P_{max}/P_y	1.06	1.10	1.06	1.67	1.99	1.81

The μ of the SFTS FEMs increased by increasing the beam L_n/d_b ratios, which indicated that the lower beam L_n/d_b ratios lead to a poor ductility capacity for the SFTS. The μ of the SFTS-BWSL FEM was obvious higher than that of the corresponding SFTS FEM. This indicated that using a shear link at a beam mid-span can improve the ductility of the SFTS.

4.3.5 Energy dissipation capacity

The dissipated energy of these FEMs calculated from the hysteretic curves is shown in Fig. 11, including the dissipated energy at each displacement level along with the total energy values. As shown in Fig. 11(a), the dissipated energy of the SFTS FEM was higher than that of the corresponding SFTS-BWSL FEM when they were loaded at the same displacement level. This is because the SFTS FEM had a higher load-carrying capacity than that of the SFTS-BWSL FEM at the same displacement level, which led to the larger hysteretic loop areas of the SFTS FEM. However, as shown in Fig. 11(b), considering the limited deformation capacity of the SFTS, the total dissipated energy of the SFTS FEM was obviously less than that of the SFTS-BWSL FEM, particularly for SFTS1 and SFTS2. This is because the SFTS-BWSL had a better ductility capacity compared to that of the corresponding SFTS. Thus, the SFTS-BWSL had a significantly better energy dissipation capacity than that of the SFTS as shown by the analytical results.

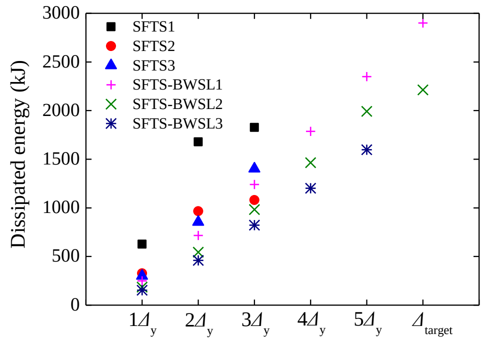

(a) Energy in each displacement level

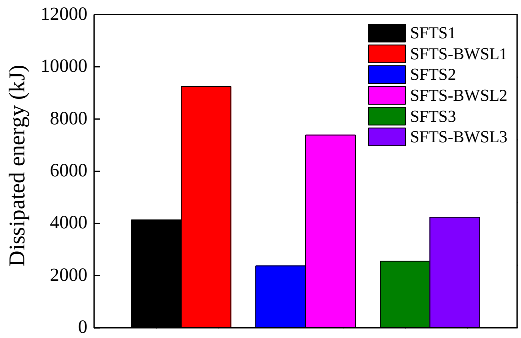

(b) Total energy

Fig. 11 Energy dissipation capacity

Table 6 Elastic stiffness of the FEMs

FEMs	Elastic stiffness K_e (kN/mm)	
	Positive direction	Negative direction
SFTS1	84.5	84.5
SFTS2	56	56
SFTS3	37.4	37.4
SFTS-BWSL1	81.5	81.8
SFTS-BWSL2	52.7	52.9
SFTS-BWSL3	34.2	34.2

Table 7 Ductility capacity of the FEMs

FEMs	Ductility coefficient μ	
	Positive direction	Negative direction
SFTS1	3.0	3.0
SFTS2	3.0	3.0
SFTS3	4.0	4.0
SFTS-BWSL1	6.0	6.0
SFTS-BWSL2	5.5	5.5
SFTS-BWSL3	5.0	5.0

4.3.6 Failure mechanism

The deformation and plastic equivalent strain (PEEQ) distributions of the SFTS and SFTS-RSL FEMs are shown in Figs. 12 and 13, respectively. In the SFTS FEMs, the yielding was at the beam-ends, column-ends near the beam-to-column connections, and beam-to-column connection zones. Compared to the PEEQ in the yield state of the SFTS

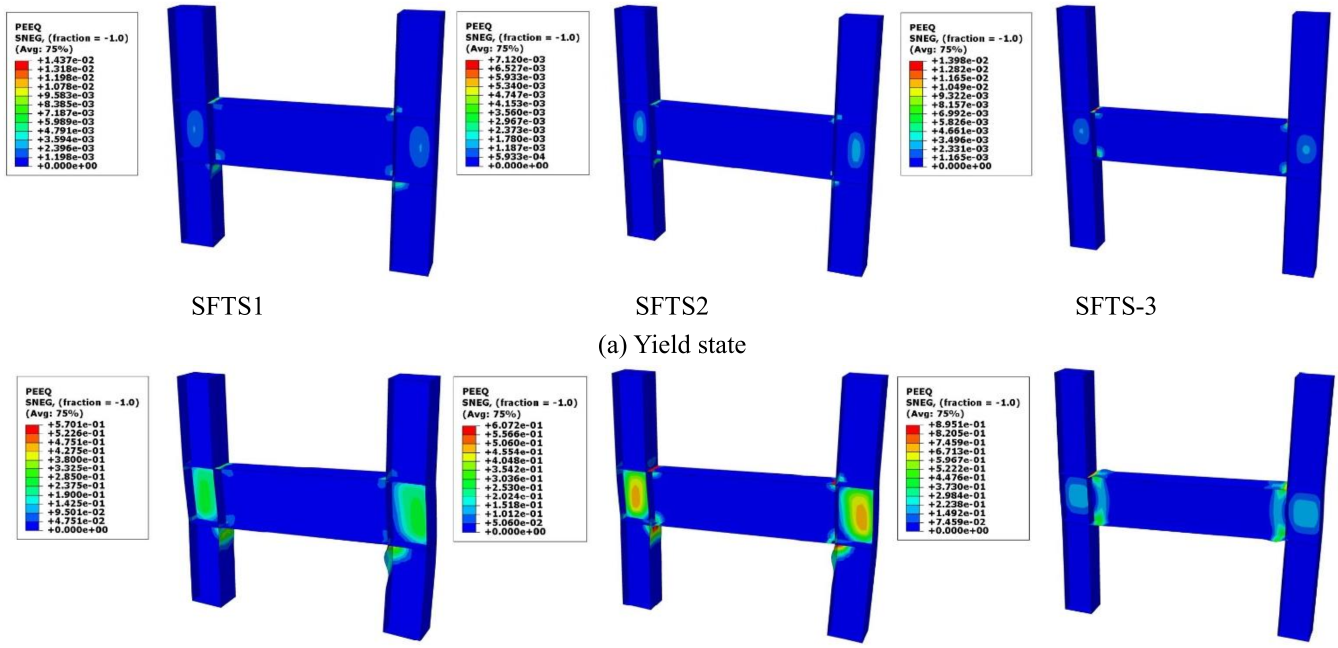

SFTS1 SFTS2 SFTS-3

(a) Yield state

SFTS1 SFTS2 SFTS3

(b) Ultimate state

Fig. 12 Distributions of PEEQ in SFTS FEMs

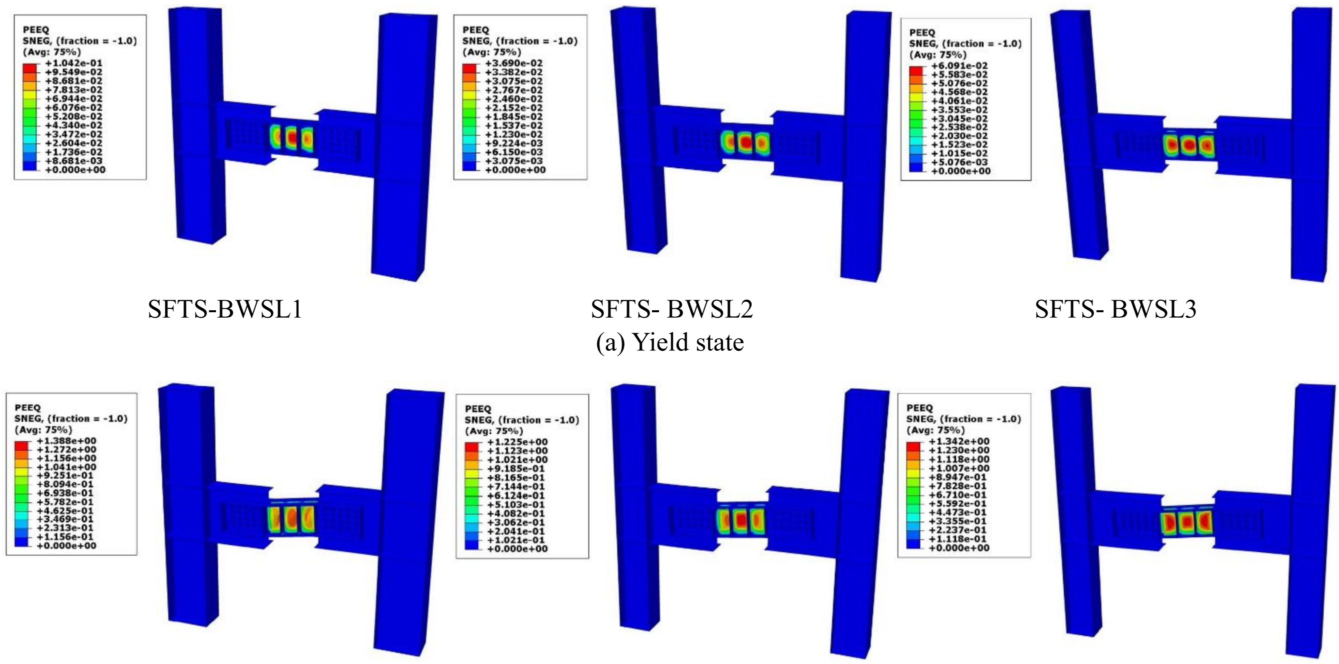

SFTS-BWSL1 SFTS- BWSL2 SFTS- BWSL3

(a) Yield state

SFTS-BWSL1 SFTS- BWSL2 SFTS- BWSL3

(b) Ultimate state

Fig. 13 Distributions of PEEQ in the SFTS-BWSL FEMs

FEMs, their beam-end plasticities did not fully develop, but the PEEQ in the column-ends and beam-to-column connection zones showed great developments. For SFTS1 and SFTS2, local buckling occurred in the flange of the column-ends, whereas it was not observed in SFTS3. This is because the great section depth of the spandrel beam results in limited development of the plastic hinge under the cyclic loads, and the energy had to be dissipated by the plastic deformation of column and beam-to-column connections in SFTS FEMs. Thus, the local buckling

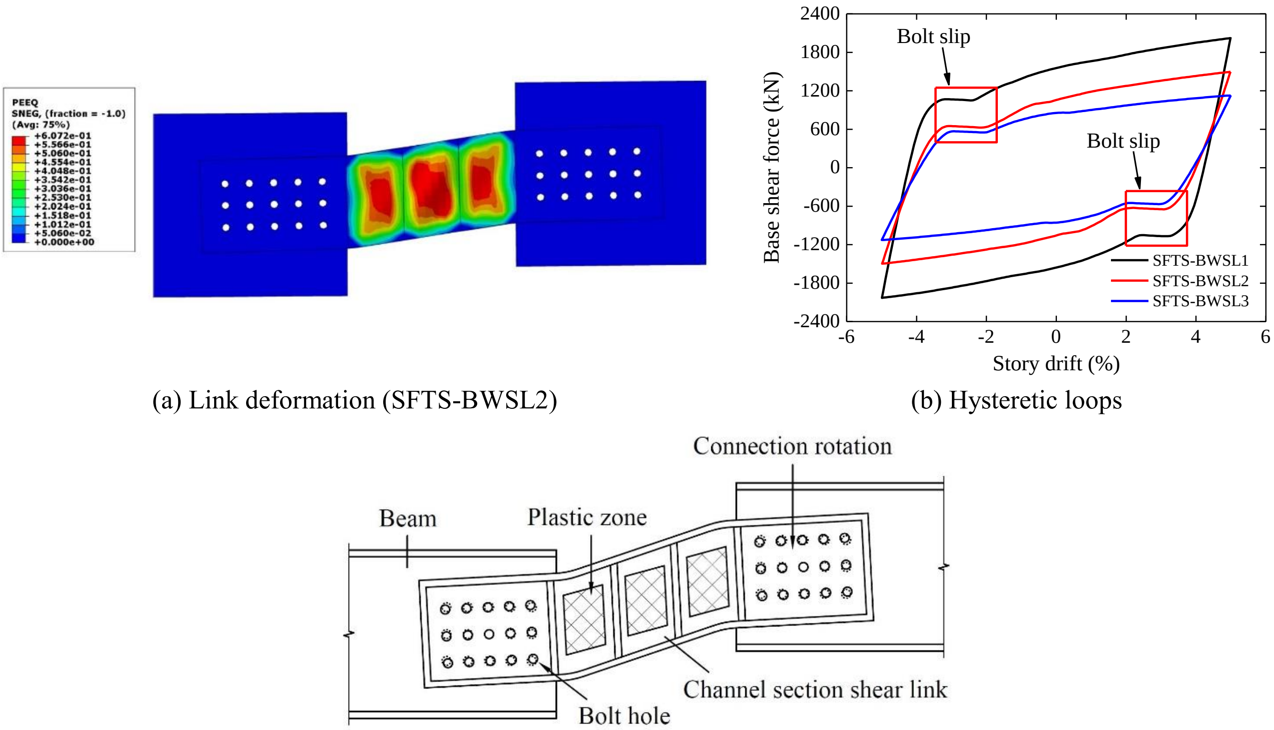

(a) Link deformation (SFTS-BWSL2)

(b) Hysteretic loops

(c) Link and connection rotations

Fig. 14 Bolted web-connected link rotations

occurred at the columns in SFTS1 and SFTS2 when these FEMs reached large displacement levels. However, the plastic deformation capacity of beam-end increases by increasing the beam span-to-depth ratios, which leads to the local buckling of beam flange caused by flexural deformation at beam-ends in SFTS3. For the web of the shear links, the cyclic shear strength caused an iterative process with tension and pressure in diagonal direction, resulting in the web buckling. This result is because the poor plastic deformation of the deep spandrel beam in the SFTS results in the higher plasticity in the column-ends; however, it was alleviated by increasing the beam L_n/d_b ratios. The lower span-to-depth ratios limit the development of plastic hinges at the beam-ends in the SFTS, leading to the lower energy dissipation capacity of the beam and the higher plasticity in the column-ends and beam-to-column connection zones. Moreover, the PEEQ in the SFTS showed that the beam with a span-to-depth ratio less than 5 can result in significant yield in the column-ends and beam-to-column connection zones, which may increase the possibility of structural collapse. When the SFTS-BWSL FEMs yielded, the plasticity developed throughout the entire web of the shear links. The beams, columns, and beam-to-column connection zones were in an elastic state. When the SFTS-BWSL FEMs reached the ultimate state, the plasticity within the web of the shear link obviously developed but no plasticity occurred in the other structural components. The plastic strain concentrated on the web of the shear link, indicating that the shear link worked as expected.

The PEEQ distributions in the SFTS-BWSL FEMs show that the plasticity concentrates on the shear link while the other structural components are in an elastic state during the seismic loads. The SFTS-BWSL can achieve the goal of seismic rehabilitation by replacing the damaged shear links with new links.

Fig. 14 shows the back-to-back double channel section bolted web-connected shear link rotations in the SFTS-BWSL. The PEEQ distribution shows that local buckling occurred in the link web and the shear plastic deformation concentrated on the link web. The hysteretic loops of SFTS-BWSL1, SFTS-BWSL2, and SFTS-BWSL3 shown in Fig. 14(b) indicated that the bolt slip occurred by increasing the horizontal displacement. Before bolt slip, the bolted web connection could be considered initially rigid because the loads transferred through the frictional force between the link and beam as a result of bolt pretensioning. The bolt slip led to connection rotations and bolts bearing on the link web, as seen in Fig. 14(c). There was no increase in the base shear force within the bolt slip because of the connection slip resistance. When the loading was reversed, considering the pretensioned bolts, the connection was rigid again until reaching the slip resistance. Then, the bolts slipped again. This result indicated that the bolt slip may result in a higher deformation and lower load-carrying capacity of the SFTS-BWSL than when using the welded connection for the shear link. However, the bolted web connection beneficial to shear link replacement following earthquakes.

5. Static and dynamic analyses

5.1 Finite element models

During the static and dynamic analyses, SAP2000 was used to establish the FEMs of the 30-story SFTS and SFTS-BWSL buildings. The designations of the two FEMs were SFTS and SFTS-BWSL, respectively. Table 8 presents the fundamental natural periods of these two FEMs, in which the differences in the periods between the SFTS-BWSL and SFTS were less than 0.5%. This shows that placing a shear link at the beam mid-span with the flexural demand resulting from the lateral load is theoretically zero and has nearly no effect on the initial lateral stiffness of the structure.

In these two FEMs, beam elements were considered for all structural components. A nominal yield strength of 345 MPa was adopted for the Q345 steel. The elastic modulus and Poisson's ratio for the steel were assumed to be 206,000 MPa and 0.3, respectively. The influence of the initial imperfections and residual stress for the FEMs was not considered and the *P*-delta effects were included in the analyses. Nonlinear hinges were defined at the links, beams, and columns. For the columns and beams, the plastic hinges were at the columns-ends and beam-ends by the plastic hinge models for the steel column and beam as shown in Tables 5 and 6 of FEMA-356, which were presented in SAP2000. The shear hinge model presented in Tables 5 and 6 of FEMA-356 was considered for the nonlinear behavior of the shear link in the positive and negative directions, as shown in Fig. 15. In this model, the ultimate shear force of the shear link was V_u=1.4V_p according to the experimental results of the shear links (Okazaki and Engelhardt 2015). In addition, considering the performance of shear link in SFTS-BWSL is similar to the EBF shear link, the research indicates that this model for shear link can effectively verify the shear plasticity and shear plastic hinge distributions on the shear link for the dynamic analysis based on the shake table test (Lian and Su 2018). Thus, in SFTS-BWSL, such nonlinear model for shear link can simulate its performance and plasticity for both static and dynamic analysis. For the shear link, the immediate occupancy deformation Δ_{IO}, life safety plastic deformation Δ_{LS}, and collapse prevention deformation Δ_{CP} were determined using the parameters suggested in Tables 5 and 6 of FEMA-356. Furthermore, in the static and dynamic analyses the life safety structural performance level as well as the nonlinear behavior of the shear link of FEMA-356 was used.

Table 8 Fundamental natural periods

SAP2000 FEMs	Period (s)		
	T_1	T_2	T_3
SFTS	3.846	3.846	2.488
SFTS-BWSL	3.863	3.863	2.502
Period difference [a]	0.44%	0.44%	0.56%

[a] refers to ($T_{SFTS\text{-}BWSL}$-T_{SFTS})/ T_{SFTS}, where $T_{SFTS\text{-}BWSL}$ and T_{SFTS} are the period of SFTS-BWSL and SFTS, respectively.

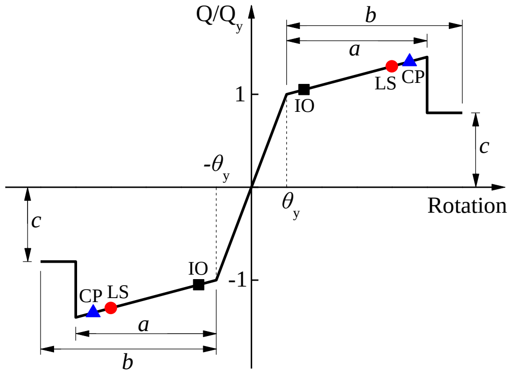

Fig. 15Generalized force–deformation relation for the shear link (FEMA-356)

5.2 Static analysis results

In the static pushover analyses for the FEMs of SFTS and SFTS-BWSL, the higher-mode displacement-controlled pattern in FEMA 274 was considered. The static pushover analyses were conducted along the x direction of the design buildings, as shown in Fig. 3. A value of 2% of the total height of the buildings (*D*/*H*=2%, where *D* and *H* are the roof displacement and total height of building, respectively) was selected as the target displacement for the static analyses. The lateral resistance performance of the SFTS and SFTS-RSL was investigated through static pushover analyses, including the lateral stiffness, load-carrying capacity, and ductility.

The static pushover curves of the static analyses for the SFTS and SFTS-BWSL FEMs are shown in Fig. 16. It shows that the SFTS-BWSL had a lower load-carrying capacity than that of the SFTS when they reached the same roof drift. However, the maximum roof drift of the SFTS was slightly higher than 1.5%, while the SFTS-BWSL could reach the target drift of 2%. This result indicates that the SFTS-BWSL had a better deformation capacity than that of the SFTS. Table 9 shows some performance parameters of the SFTS and SFTS-BWSL, including the initial lateral stiffness K_e, yield strength P_y, maximum load-carrying capacity P_{max}, yield roof drift θ_y, and maximum roof drift θ_{max}. The SFTS-BWSL and SFTS had nearly the same K_e values, which indicated that placing a shear link at the mid-span of the beam had nearly no effect on the initial elastic lateral stiffness of the structure. Compared to the SFTS-BWSL, the SFTS had a much higher P_y, which was 37.6% higher than that of the SFTS-BWSL. However, the P_{max} of the SFTS-BWSL was only 9% less than that of the SFTS. The P_{max}/P_y of the SFTS-BWSL was 1.5, which was higher than the 1.2 of the SFTS. This result shows that the SFTS-BWSL had a more stable hardening behavior than that of the SFTS. The ductility coefficient μ of the SFTS-BWSL was 1.8 times higher than that of the SFTS, indicating that the SFTS-BWSL had better ductility.

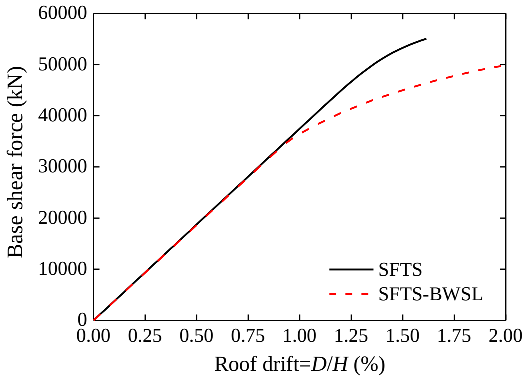

Fig. 16 Base shear force-roof drift curves

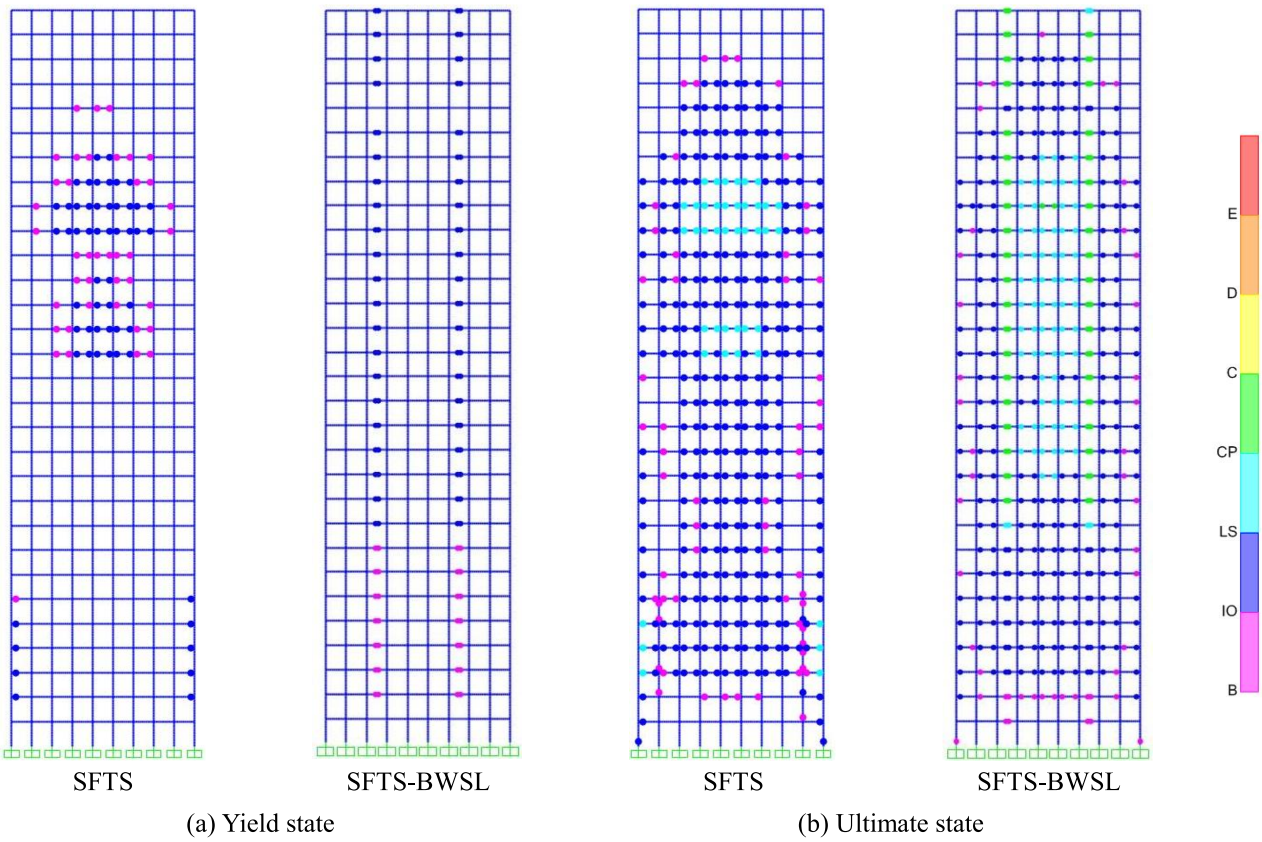

Fig. 17 Plastic hinge distributions

Table 9 Load-carrying capacity and ductility

FEMs	SFTS	SFTS-BWSL
K_e (kN/mm)	40.0	39.8
P_y (kN)	47378.6	34427.8
P_{max} (kN)	55073.0	49904.8
θ_y (%)	1.3	0.9
θ_{max} (%)	1.6	2.0
P_{max}/P_y	1.2	1.4
$\mu=\theta_{max}/\theta_y$	1.2	2.2

The plastic hinge distributions of the SFTS and SFTS-BWSL at the yield and ultimate states are shown in Figs. 17(a) and 17(b), respectively. The plastic hinges were mainly observed at the beam-ends in the upper stories and a few were at the beam-ends in the lower stories when the SFTS reached the yield state. It shows that nearly all shear links had plasticity and there was a uniform plastic hinge distribution with shear links yielding when the SFTS-BWSL yielded. When the SFTS-BWSL reached the ultimate state, all shear links were in a plastic state and for the plastic hinges observed at the shear links and beam-ends, only some were observed at the column-ends of the bottom corner columns. When the SFTS reached the

Table 10 Characteristics of ground motions

Earthquakes	Year	Station	Record	Pr. of exc. (% in 50 yrs)	Magnitude	Source distance (km)	*PGA* (g)	*PGV* (cm/s)	Scale factors
Chi-Chi, Taiwan	1999	TCU095	ChiChi/TCU095-W	50/10/2	7.6	43.4	0.379	62	0.29/0.79/1.35
Northridge	1994	Castaic-Old Ridge Route	NORTHR/ORR090	50/10/2	6.7	20.1	0.568	52.1	0.19/0.53/0.90
Superstitn Hills	1987	El Centro Imp. Co. Cent	SUPERST/B-SUP135	50/10/2	6.5	5.6	0.894	42.2	0.12/0.34/0.57
Imperial Valley	1979	Delta	IMPVALL/H-DLT352	50/10/2	6.53	12.45	0.24	26.0	0.29/0.83/1.67
Loma Prieta	1989	CDMG 47381 Gilroy Array #3	LOMAP/G03000	50/10/2	6.93	12.82	0.56	35.6	0.13/0.36/0.71
Cape Mendocino	1992	Rio Dell Overpass	CAPEMEND/RIO360	50/10/2	7.01	14.33	0.39	44.1	0.18/0.51/1.03
Landers	1992	Yermo Fire Station	LANDERS/YER360	50/10/2	7.28	23.62	0.24	51.4	0.29/0.83/1.67
Kern County	1952	Taft Lincoln School	KERN/TAF021	50/10/2	7.4	41	0.156	15.3	0.71/1.92/3.27
Kobe, Japan	1995	Shin-Osaka	KOBE/SHI090	50/10/2	6.9	19.15	0.24	37.8	0.29/0.83/1.67
Duzce, Turkey	1999	Bolu	DUZCE/BOL090	50/10/2	7.14	12.04	0.73	56.4	0.10/0.27/0.55

ultimate state, the plastic hinges were mostly distributed at the beam-ends, but the plastic hinges were observed at column-ends in some stories. It is noticeable that the developments of the plastic hinges were limited in the SFTS and were obviously lower than those in the SFTS-BWSL.

5.3 Dynamic analyses and results

5.3.1 Ground motions

Dynamic analyses were considered in this study to investigate and compare the seismic performance of the SFTS and SFTS-BWSL FEMs using a set of ground motions. The ground motions were selected based on the ground conditions and the properties of earthquakes, including the spectra characteristics, magnitudes, accelerations, velocities, and durations, which can be summarized as: (1) The ground conditions for the 30-story structures and ground motions are similar; (2) For the ground motions, the Magnitude $M > 5$, $PGA > 0.1$ g, PGV (peak ground velocity) > 20 cm/s, t (duration) > 30 s; (3) The differences between the response spectra of ground motions and the design spectra for 30-story structures are lower than 25% within [0.1, T_g], where T_g is the characteristic period rely on the ground conditions in GB50011-2010. In particular, the accelerations of earthquakes may be the most critical for structural dynamics. Therefore, the selections of accelerations for these ground motions could be carried out through the critical excitation method (Kamgar and Rahgozar 2015, Kamgar *et al.* 2018). In this study, ten ground motions were selected, including near-filed and far-field earthquakes, which are shown in Table 10. In addition, three levels of seismic hazard were considered for the selected ground motions as follows: 50%, 10%, and 2% probability of exceedance during a 50-year period. The loading direction for the dynamic loads was the x-direction of the structure, as shown in Fig. 3. For the dynamic analyses, the ground motions with a probability exceedance of 50%, 10%, and 2% during a 50-year period were defined as frequent, moderate, and severe earthquakes. Considering the PGAs for frequent, moderate, and severe earthquakes are 0.07, 0.2, and 0.4 g, respectively, in JGJ99-2015, the earthquake scale factors in Table 10 were defined to scale the PGAs of these selected ground motions to the corresponding PGAs of the three level earthquakes. Fig. 18 shows the acceleration response spectra of the ensemble of the accelerograms and the design acceleration spectrum.

5.3.2 Dynamic analysis results

The comparisons of mean maximum interstory drift between the SFTS and SFTS-BWSL FEMS during the three earthquakes are shown in Fig. 19. It shows that the interstory drifts of the two FEMs increased by increasing the earthquake intensities. The interstory drifts of the SFTS-BWSL were lower than the corresponding drifts of the SFTS during the different earthquakes.

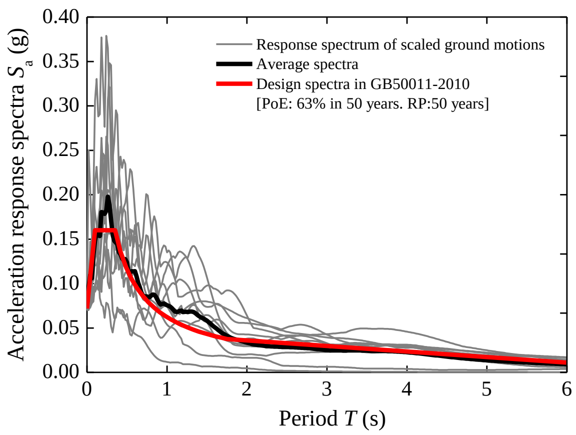

Fig. 18 Design spectra and scaled earthquake spectra

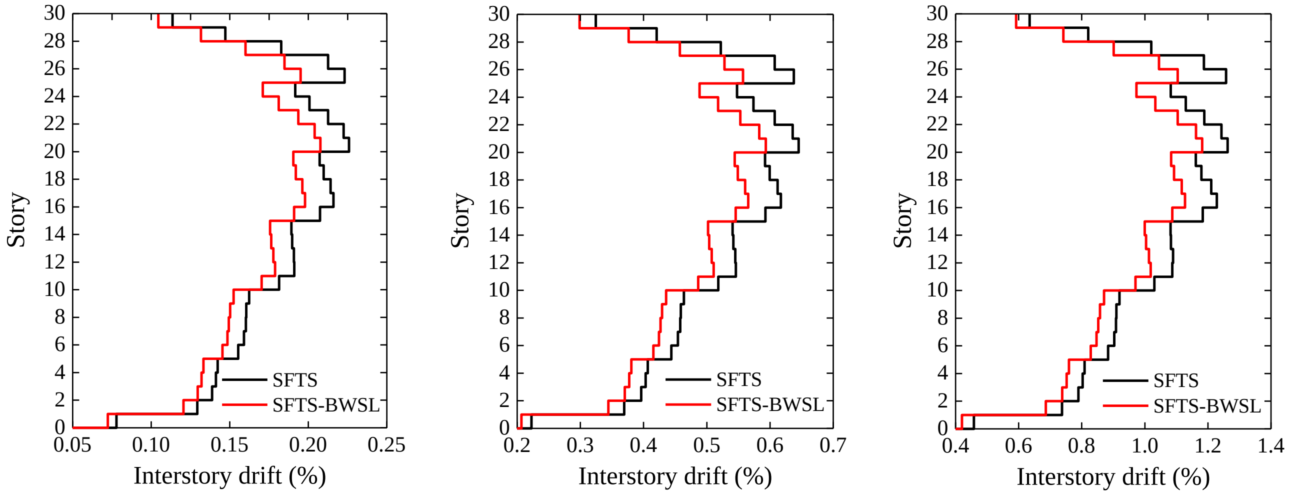

(a) Frequent earthquakes (b) Moderate earthquakes (c) Severe earthquakes

Fig. 19 Interstory drift comparisons

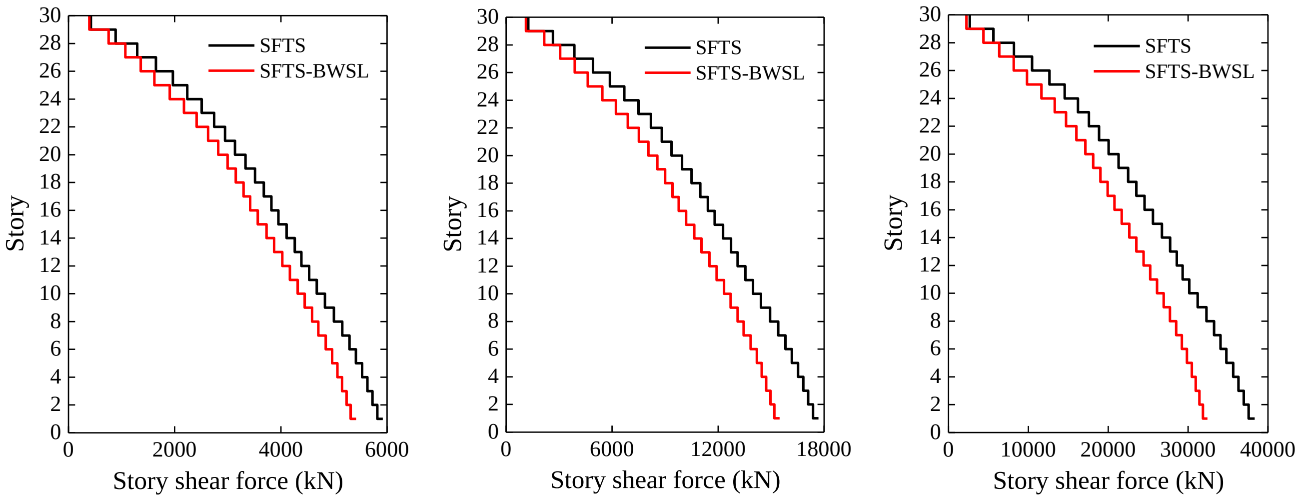

(a) Frequent earthquakes (b) Moderate earthquakes (c) Severe earthquakes

Fig. 20 Story shear force comparisons

The difference in the mean maximum interstory drift between the SFTS-BWSL and SFTS was 13.1% during the frequent earthquakes. For the moderate and severe earthquakes, the differences were 14.3% and 14.1%, respectively. During the moderate and severe earthquakes, the mean maximum interstory drifts of the SFTS and SFTS-BWSL were much less than the interstory drift limitation of 2%. The interstory drift comparisons of the SFTS and SFTS-BWSL show that the SFTS-BWSL had lower interstory drifts than those of the SFTS during the earthquake loads of different intensities. This result indicates that using a shear link at the mid-span of the beam will not increase but decrease the interstory drift of the structure during earthquakes.

Fig. 20 shows the story shear force comparisons of the SFTS and SFTS-BWSL during the three earthquakes, in which the story shear force of the SFTS-BWSL was significantly less than that of the SFTS. The mean maximum story shear force of the SFTS-BWSL was 17.7% less than the corresponding story shear force of the SFTS during frequent earthquakes. For moderate and severe earthquakes, the differences were 21.3% and 22.4%, respectively. Table 11 presents the mean maximum base shear force $P_{max,m}$ of the SFTS and SFTS-BWSL under the earthquake loads of different intensities. It shows that the SFTS-BWSL had a lower $P_{max,m}$ than that of the SFTS. The difference in the $P_{max,m}$ between the SFTS-RSL and SFTS obviously increased relative to the earthquake intensity, which ranged from 9.3% to 18.2%. The SFTS-BWSL had a lower story shear force and base shear force than that of the SFTS during the earthquake loads which indicated the lower earthquake responses of the SFTS-BWSL, which is of benefit in reducing earthquake damage to the structure.

Table 11 Mean maximum base shear force comparison of the SFTS and SFTS-RSL

FEMs	Mean maximum base shear force $P_{max,m}$ (kN)	
	Frequent earthquakes	Moderate earthquakes
SFTS	5919.3	17680.8
SFTS-BWSL	5416.7	15473.2
Base shear force difference [a]	9.3%	14.3%

[a] refers to $(P_{SFTS\text{-}BWSL}-P_{SFTS})/P_{SFTS}$, where $P_{SFTS\text{-}BWSL}$ and P_{SFTS} are the base shear force of SFTS-BWSL and SFTS, respectively

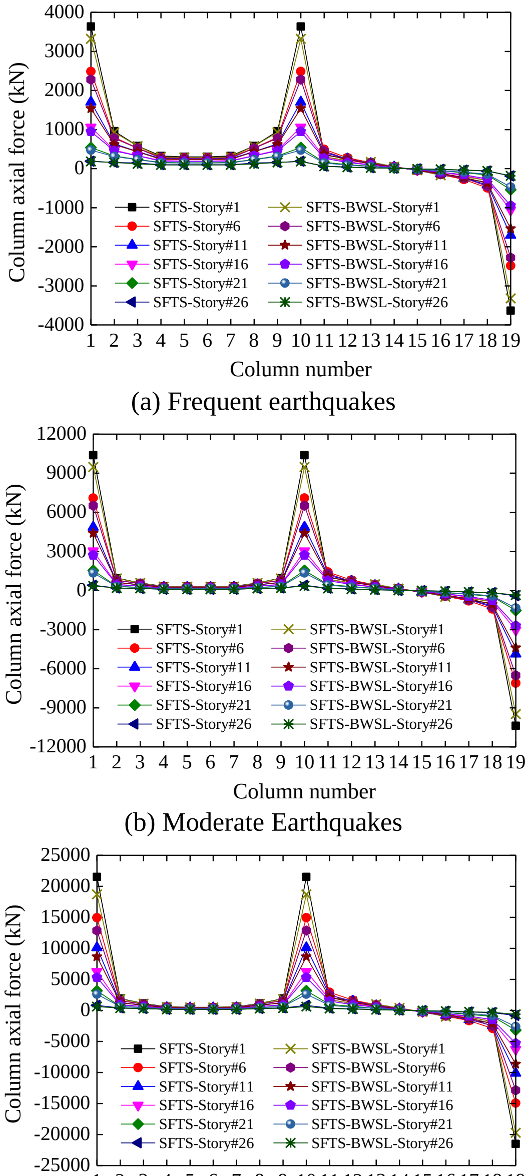

(a) Frequent earthquakes

(b) Moderate Earthquakes

(c) Severe earthquakes

Fig. 21 Columns axial force comparison of SFTS and SFTS-BWSL

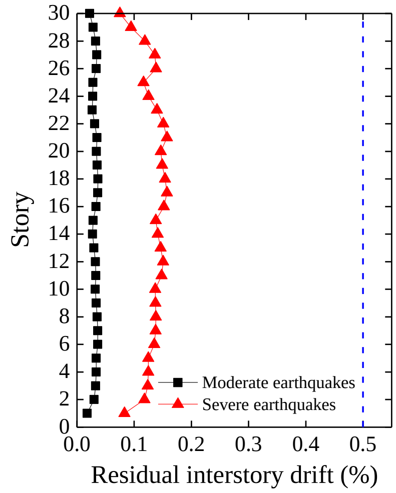

Fig. 22 Residual interstory drifts of the SFTS-BWSL

The mean column axial force comparisons of the SFTS and SFTS-BWSL during different ground motions are shown in Fig. 21, including the axial force of the columns on the 1st, 6th, 11th, 16th, 21st, and 26th stories; the column numbers are presented in Fig. 3. In the web frame (x-direction of the building as shown in Fig. 3), the SFTS-BWSL had a lower column axial force than that of the SFTS. For frequent earthquakes, the differences in the column axial forces between the SFTS-BWSL and SFTS ranged from 0.8% to 21.3%. For the moderate and severe earthquakes, the differences ranged from 3.1% to 21.9% and from 6.0% to 27.8%, respectively. This result indicated that the differences in the column axial force were significant in the bottom stories. However, in the flange frame (y direction of the building as shown in Fig. 3), the SFTS and SFTS-BWSL had a similar column axial force as that of columns 1# to 10# during the three earthquakes. The comparisons of the column axial force between the SFTS and SFTS-BWSL show that placing a shear link at the mid-span of the beam could not increase the shear lag effects to the steel framed-tube structure.

Fig. 22 shows the mean residual interstory drifts of the SFTS-BWSL after the moderate and severe earthquakes. McCormick et al. showed that a residual drift of 0.5% represents a limit beyond which it is more economical to rebuild a structure than it is to repair it (McCormick et al. 2008). However, the maximum residual story drifts of the SFTS-RSL were 0.04% and 0.16% after the moderate and severe earthquakes, respectively, which were much less than the residual drift of 0.5%. For the shear links in the SFTS-BWSL, 0.02 rad is the residual link rotation angle corresponding to the residual interstory drift of 0.5%. The maximum residual rotational angle of the shear links in the SFTS-BWSL was 0.002 and 0.007 rad for the moderate and severe earthquakes, respectively, much less than the 0.02 rad. This result indicates that the SFTS-BWSL can be repaired by replacing the damage shear links after earthquakes.

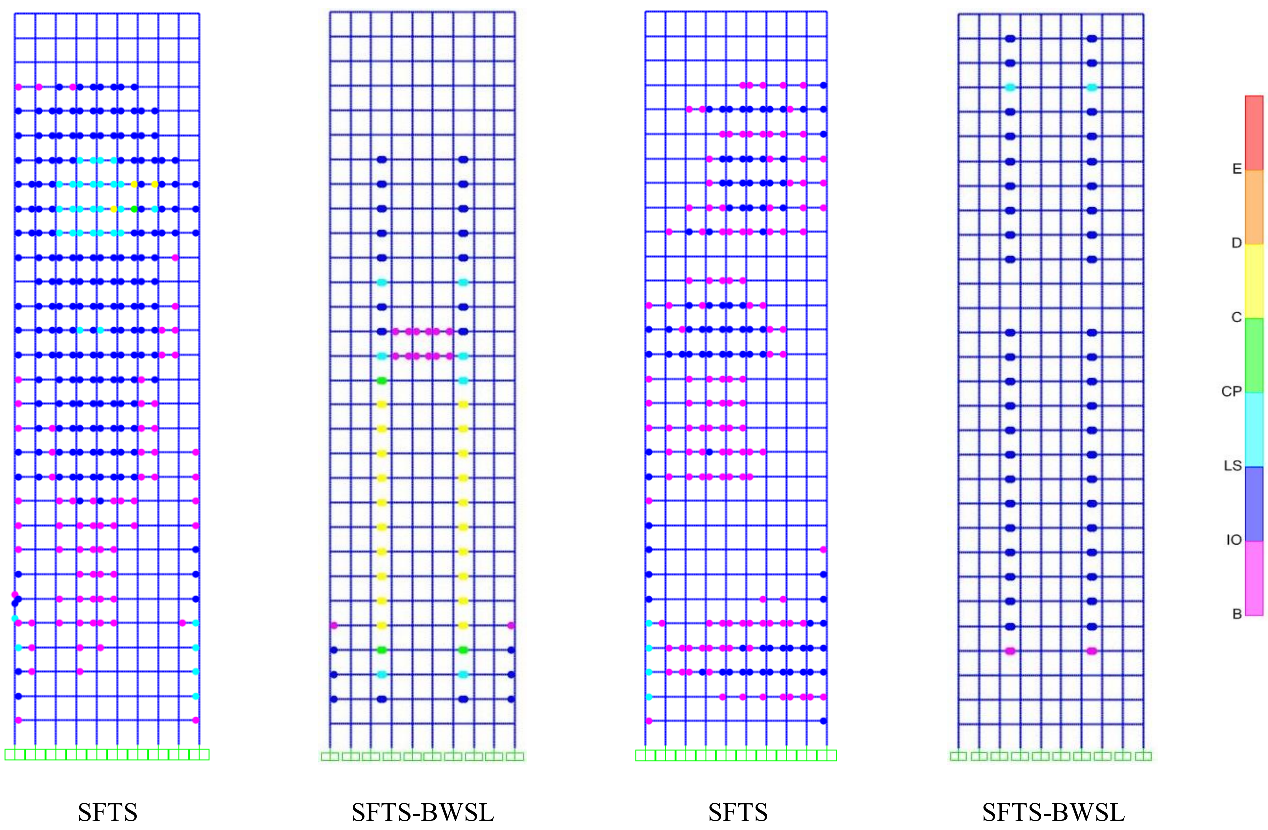

(a) Kobe (b) Chi-Chi

Fig. 23 Plastic hinge distributions during the severe earthquakes

Fig. 23 shows the plastic hinge distributions of the SFTS and SFTS-BWSL during the severe Kobe and Chi-Chi earthquakes. It shows that the SFTS had many more plastic hinges than that of the SFTS-BWSL. These were mostly observed at the beam-ends with some at the column-ends of the lower stories in the SFTS. It is noticeable that many plastic hinges at the beam-ends reached the state of collapse prevention (CP) in the SFTS, particularly in the upper stories. This increased the difficulties in post-earthquake repairing. In the SFTS-BWSL, the plastic hinges were mostly observed at the shear links except for some obverted on the beam-ends during the Kobe earthquake. However, the plastic hinges on the beam-ends only yielded and the development of the plastic hinges on the shear links was much higher. The SFTS-BWSL dissipated the earthquake energy via link plastic shear deformation and the other components were nearly still in the elastic state, which indicates that the SFTS-BWSL is a reliable seismic-resistant system. Moreover, replacing the damaged shear links with new links can achieve the goal of seismic rehabilitation for the SFTS-BWSL.

6. Summaries

The seismic behaviors of the SFTS and SFTS-BWSL were compared by hysteretic, static pushover, and dynamic analyses. The results show that the SFTS-BWSL is a reliable seismic resistant system with better ductility and energy dissipation capacities and it offers the ability to repair the structure by replacing the damaged shear links after earthquakes. In SFTS, deep spandrel beams typically have the span-to-depth ratios lower than 5.0. The moment demands have a sharp gradient across the span, which results in the plastic hinge at beam-end can not have a sufficient length and reduces the plastic deformation of flexural beam. However, the shear demands are increasing and significant due to decreasing the span-to-depth ratio of beam and the moment demands at the mid-span of the spandrel beam are theoretical zero. Thus, the bolted web-connected shear link can provide enough shear and energy dissipation capacity, but does not significantly reduce the lateral stiffness. This can improve the ductility and energy dissipation capacities of the SFTS.

According to the numerical analysis results, the strong sides of SFTS-BWSL can be summarized as follows:

(1) The SFTS-BWSL has better ductility and energy dissipation capacities than those of the SFTS, showing that using the bolted web-connected shear link at the beam mid-span can improve the ductility and energy dissipation capacities of the SFTS efficiently.

(2) The SFTS-BWSL has lower dynamic responses than those of the SFTS during earthquakes with different intensities, including interstory drift, story shear force, and base shear force.

(3) In the SFTS-BWSL, the plasticity concentrates on

the shear link and the shear plastic hinges show significant improvement. The earthquake energy is dissipated via the shear deformation of the links, such that the other structural components are in elastic states.

(4) The residual story drifts of SFTS-BWSL are less than 0.2% under the severe earthquakes. It shows that replacing shear links is allowable and the expected post-earthquake recoverability and resilience of SFTS-BWSL can be achieved.

In addition, the strong sides of SFTS-BWSL can be summarized as follows:

(5) The SFTS-BWSL has a lower lateral strength carrying capacity than that of the SFTS, including the yield and maximum strength. This is because the shear capacity of shear link is lower than that of deep spandrel beam.

The numerical analysis results show that using a bolted web-connected replaceable shear link with a back-to-back double channel section at the mid-span of deep spandrel beam has a slight effect on the initial lateral stiffness, and can obviously improve the ductility and energy dissipation capacities of a SFTS with beam span-to-depth ratios of from 3.0 to 4.0. However, the flexural deformation capacities of beams increase with the increasing beam span-to-depth ratios, reducing the advantages of ductility and energy dissipation capacities of SFTS-BWSL. Therefore, the proposed methodology that placing a bolted web-connected shear link at the mid-span of the beam with span-to-depth ratio less than 4.0, can significantly improve the ductility and energy dissipation capacities of an SFTS.

7. Conclusions

In the SFTS, the characteristic of the deep spandrel beams with low span-to-depth ratios leads to lower structure ductility and energy dissipation capacities. The bolted web-connected replaceable shear link with a back-to-back double channel section was proposed as the ductile fuse at the mid span of a deep spandrel beam to improve the seismic behavior of the SFTS and the earthquake energy can be dissipated by the shear plasticity of the link. Two 30-story buildings were designed, including one with a SFTS and one with a SFTS-BWSL. Several SFTS and SFTS-BWSL sub-structures were selected from the two buildings to investigate their hysteretic performance. Static pushover and nonlinear dynamic analyses were conducted to study and compare the seismic responses of the two buildings. The following conclusions can be drawn within the limitations of the research:

(6) Placing a bolted web-connected shear link with back-to-back double channel sections at the mid-span of deep spandrel beam can improve the ductility and energy dissipation capacities of SFTS. In SFTS-BWSL, the shear links entered plastic stage to dissipate energy while spandrel beam and columns remained in elastic stage under the seismic loads. The SFTS-BWSL develops the expected ductile failure mode.

(7) The SFTS-BWSL and SFTS have similar initial lateral stiffness and shear lag effects. Compared to the SFTS, SFTS-BWSL has lower yield and maximum strengths but improved hardening behaviors and ductility and energy dissipation capacities under the cyclic loads. Moreover, the SFTS-BWSL has lower dynamic responses than those of the SFTS during earthquakes, including interstory drifts, story shear force, and base shear force.

(8) During earthquakes, the the residual story drifts of the SFTS-BWSL are much lower than 0.5%, which suggests that the SFTS-BWSL is a reliable seismic-resistant system that can be repaired by replacing the damaged shear links after earthquakes. Therefore, the expected post-earthquake recoverability and resilience of the structures can be achieved.

(9) According to the numerical analysis results, placing a bolted web-connected shear link at the mid-span of a beam can significantly improve the ductility and energy dissipation capacities of the SFTS when the beam span-to-depth ratios are less than 4.0.

Acknowledgements

The authors are grateful for the partial financial support from the National Natural Science Foundation of China (Grant No. 51708444), Shaanxi Natural Science Foundation (Grant No. 2018JQ5074), and scientific research plan projects of Shaanxi Education Department (Grant No.18JK0456).

References

AISC 358-10 (2010), Prequalified connections for special and intermediate steel moment frames for seismic applications; Chicago, USA.

AISC 358-16 (2016), Prequalified connections for special and intermediate steel moment frames for seismic applications; Chicago, USA.

Alavi, A., Rahgozar, P. and Rahgozar, R. (2018), "Minimum-weight design of high-rise structures subjected to flexural vibration at a desired natural frequency", *Struct. Des. Tall Spec. Build.*, **27**(15), e1515. DOI: 10.1002/tal.1515.

Berman, J. W. and Bruneau, M. (2008), "Tubular links for eccentrically braced frames. I: finite element parametric study", *J. Struct. Eng.*, **134**(5), 692-701. DOI: 10.1061/(asce)0733-9445(2008)134:5(692).

Chacón, R., Vega, A. and Mirambell, E. (2019). "Numerical study on stainless steel I-shaped links on eccentrically braced frames", *J. Constr. Steel Res.*, **159**, 67-80. DOI: 10.1016/j.jcsr.2019.04.014.

Charney, F.A. and Pathak, R. (2008), "Sources of elastic deformation in steel frame and framed-tube structures: part 1: simplified subassemblage models", *J. Constr. Steel Res.*, **64**(1), 87-100. DOI: 10.1016/j.jcsr.2007.05.008.

Charney, F.A. and Pathak, R. (2008), "Sources of elastic deformations in steel frame and framed-tube structures: part 2: detailed subassemblage models" *J. Constr. Steel Res.*, **64**(1), 101-117. DOI: 10.1016/j.jcsr.2007.05.007.

Dolatshahi K.M., Gharavi, A. and Mirghaderi, S.R. (2018), "Experimental investigation of slitted web steel moment resisting frame", *J. Constr. Steel Res.*,**145**, 438-448. DOI: 10.1016/j.jcsr.2018.03.004

Dusicka, P., Itani, A.M. and Buckle, I.G. (2010), "Cyclic behavior of shear links of various grades of plate steel", *J. Struct. Eng.*, **136**(4), 370-378. DOI: 10.1061/(ASCE)ST.1943-

541X.0000131.

El-Khoriby, S., Sakr M.A., Khalifa, T.M. and Eladly, M.M. (2017), "Modelling and behaviour of beam-to-column connections under axial force and cyclic bending", *J. Constr. Steel Res.*, **129**, 171-184. DOI: 10.1016/j.jcsr.2016.11.006.

Ellingwood, B.R. (2001), "Earthquake risk assessment of building structures", *Reliab. Eng. Syst. Safe.*, **74**(3), 251-262. DOI: 10.1016/S0951-8320(01)00105-3.

Erfani, S., Asnafi, A.A. and Goudarzi, A. (2016), "Connection of I-beam to box-column by a short stub beam", *J. Constr. Steel Res.*, **127**, 136-150. DOI: 10.1016/j.jcsr.2016.07.025.

Fanaie, N. and Moghadam, H.S. (2019), "Experimental study of rigid connection of drilled beam to CFT column with external stiffeners", *J. Constr. Steel Res.*, **153**, 209-221. DOI: 10.1016/j.jcsr.2018.10.016.

FEMA (1997), NEHRP commentary on the guidelines for the seismic rehabilitation of buildings, FEMA-274, Federal Emergency Management Agency (FEMA); Washington D C, USA.

FEMA (2000), Prestandard and commentary for the seismic rehabilitation of buildings, FEMA-356, Federal Emergency Management Agency (FEMA); Washington D C, USA.

FEMA (2000), State of the art report on connection performance, FEMA-355D, Federal Emergency Management Agency (FEMA); Washington D C, USA.

GB50011-2010 (2010), Code for seismic design of buildings; Beijing, China.

GB50017-2017 (2017), Code for design of steel structures; Beijing, China.

Hu, F., Shi, G., Bai, Y. and Shi, Y. (2014), "Seismic performance of prefabricated steel beam-to-column connections", *J. Constr. Steel Res.*, **102**, 204-216. DOI: 10.1016/j.jcsr.2014.07.012.

Ji, X., Wang, Y., Ma, Q. and Okazaki, T. (2017), "Cyclic behavior of replaceable steel coupling beams", *J. Struct. Eng.*, **143**(2), 04016169. DOI: 10.2749/222137815815775934.

Jiang, Z., Yang, X., Dou, C., Li, C. and Zhang, A. (2019), "Cyclic testing of replaceable damper: Earthquake-resilient prefabricated column-flange beam-column joint", *Eng. Struct.*, **183**, 922-936. DOI: 10.1016/j.engstruct.2019.01.060.

JGJ 99-2015 (2015), Technical specification for steel structure of tall buildings; Beijing, China.

Kamgar, R. and Rahgozar, R. (2013), "A simple approximate method for free vibration analysis of framed tube structures", *Struct. Des. Tall Spec. Build.*, **22**(2), 217-234. DOI: 10.1002/tal.680.

Kamgar, R. and Rahgozar, R. (2015), "Determination of critical excitation in seismic analysis of structures", *Earthq. Struct.*, **9**(4), 875-891. DOI: 10.12989/eas.2015.9.4.875.

Kamgar, R., Samea P. and Mohsen, K. (2017). "Optimizing parameters of tuned mass damper subjected to critical earthquake", *Struct. Des. Tall Spec. Build.*, **27**(10), e1460. DOI: 10.1002/tal.1460.

Kamgar, R., Rahgozar, R. and Tavakoli, R. (2018), "The best location of belt truss system in tall buildings using multiple criteria subjected to blast loading", *Civil Eng. J.*, **4**(6), 1338-1353. DOI: 10.28991/cej-0309177.

Kamgar, R. and Rahgozar, P. (2019), "Reducing static roof displacement and axial forces of columns in tall buildings based on obtaining the best locations for multi-rigid belt truss outrigger systems", *Asian J. Civil Eng.*, **20**(6), 759-768. DOI: 710.1007/s42107-019-00142-0.

Lee, K.K., Loo, Y.C. and Guan, H. (2001), "Simple analysis of framed-tube structures with multiple internal tubes", *J. Struct. Eng.*, **127** (4), 450-460. DOI: 10.1061/(asce)0733-9445(2001)127:4(450).

Lian, M., Su, M.Z. and Guo, Y. (2017), "Experimental performance of Y-shaped eccentrically braced frames fabricated with high strength steel", *Steel Compos. Struct.*, **24**(4), 441-453. https://doi.org/10.12989/scs.2017.24.4.441 .

Lian, M. and Su, M. Z. (2018). "Seismic testing and numerical analysis of Y-shaped eccentrically braced frame made of high-strength steel", *Struct. Des. Tall Spec. Build.*, e1455. DOI: 10.1002/tal.1455

Mahmoudi, F., Dolatshahi, K.M., Mahsuli, M., Shahmohammadi, A., Nikoukalam, M.T. and Student, M.S., *et al*. (2016), "Experimental evaluation of steel moment resisting frames with a nonlinear shear fuse", *Asce Geotech. Struct. Eng. Congress*.

Malekinejad, M., Rahgozar, R., Malekinejad, A. and Rahgozar, P. (2016). "A continuous-discrete approach for evaluation of natural frequencies and mode shapes of high-rise buildings", *Int. J. Adv. Struct. Eng.*, **8**(3), 269-280. DOI: 10.1007/s40091-016-0129-6.

Mansour, N., Christopoulos, C. and Tremblay, R. (2011), "Experimental validation of replaceable shear links for eccentrically braced steel frames", *J. Struct. Eng.*, **137**(10), 1141-1152. DOI: 10.1061/(ASCE)ST.1943-541X.0000350.

McCormick, D., Aburano, H., Ikenaga, M. and Nakashima, M. (2008), "Permissible residual deformation level for building structures considering both safety and human elements", *Proceedings of the 14th World Conf. on Earthquake Engineering*, Beijing.

Mohammadrezapour, E. and Danesh, F. (2018), "Experimental investigation of bolted link-to-column connections in eccentrically braced frames", *J. Constr. Steel Res.*, **147**, 236-246. DOI: 10.1016/j.jcsr.2018.04.009.

Moon, K.S. (2010), "Stiffness-based design methodology for steel braced tube structures: a sustainable approach", *Steel Constr.*, **32**(10), 3163-3170. DOI: 10.1016/j.engstruct.2010.06.004.

Oh, K., Lee, K., Chen, L., Hong, S.B. and Yang, Y. (2015), "Seismic performance evaluation of weak axis column-tree moment connections with reduced beam section", *J. Constr. Steel Res.*, **105**, 28-38. DOI: 10.1016/j.jcsr.2014.10.005.

Ohsaki, M. and Nakajima, T. (2012), "Optimization of link member of eccentrically braced frames for maximum energy dissipation", *J. Constr. Steel Res.*, **75**, 38-44. DOI: 10.12989/scs.2018.28.2.123.

Okazaki, T. and Engelhardt, M.D. (2015), "Cyclic loading behavior of EBF links constructed of ASTM A992 steel", *J. Constr. Steel Res.*, **63**(6), 751-765. DOI: 10.1016/j.jcsr.2012.03.008.

Prinz, G.S. and Richards, P.W. (2009), "Eccentrically braced frame links with reduced web sections", *J. Constr. Steel Res.*, **65**, 1971-1978. DOI: 10.1016/j.jcsr.2009.04.017.

Rahgozar, R., Ahmadi, A.R., Ghelichi, M., Goudarzi, Y., Malekinejad, M. and Rahgozar, P. (2014). "Parametric stress distribution and displacement functions for tall buildings under lateral loads", *Struct. Des. Tall Spec. Build.*, **23**(1), 22-21. DOI: 10.1002/tal.1016

Shayanfar, M.A., Barkhordari, M.A. and Rezaeian, A.R. (2012), "Experimental study of cyclic behavior of composite vertical shear link in eccentrically braced frames", *Steel Compos. Struct.*, **12**(1), 13-29. https://doi.org/10.12989/scs.2012.12.1.013

Silvia, C., Nicola, M. and Walter, S. (2018), "Experimental and numerical assessment of EBF structures with shear links" , *Steel Compos. Struct.*, **28**(2), 123-138. https://doi.org/10.12989/scs.2018.28.2.123.

Sophianopoulos, D.S. and Deri, A.E. (2017), "Steel beam-to-column RBS connections with European profiles: I. Static optimization", *J. Constr. Steel Res.*, **139**, 101-109 DOI: 10.1016/j.jcsr.2017.09.028

Taranath, B.S. (2011), "Structural analysis and design of tall buildings: steel and composite construction", CRC Press 2011.

Zhang, The structural design of tall and special buildings, 2018;

e1455.
Wang, A., Jiang, Z.Q., Yang, X. and Zhang, H. (2019), "Experimental study of earthquake-resilient prefabricated steel beam-column joints with different connection forms", *Eng. Struct.*, **187**, 299-313. DOI: 10.1016/j.engstruct.2019.02.071.

CC